Geochemistry, Geophysics, Geosystems®

RESEARCH ARTICLE
10.1029/2023GC011396

Special Section:
Advances in understanding volcanic processes

Magma Differentiation in Dynamic Mush Domains From the Perspective of Multivariate Statistics: Open- Versus Closed-System Evolution

A. Pontesilli[1], F. Di Fiore[1], P. Scarlato[1], B. Ellis[2], E. Del Bello[1], D. Andronico[3], J. Taddeucci[1], M. Brenna[4], M. Nazzari[1], O. Bachmann[2], and S. Mollo[1,5]

[1]Istituto Nazionale di Geofisica e Vulcanologia, Roma, Italy, [2]Institute of Geochemistry and Petrology, ETH Zurich, Zurich, Switzerland, [3]Istituto Nazionale di Geofisica e Vulcanologia-Osservatorio Etneo, Catania, Italy, [4]Department of Geology, University of Otago, Dunedin, New Zealand, [5]Dipartimento di Scienze della Terra, Sapienza Università di Roma, Roma, Italy

Abstract Open-conduit conditions characterize several of the most hazardous and active volcanic systems of basaltic composition worldwide, persistently refilled by magmatic inputs. Eruptive products with similar bulk compositions, chemically buffered by continual mafic inputs, nevertheless exhibit heterogeneous glass compositions in response to variable magma mixing, crystallization, and differentiation processes within different parts of the plumbing system. Here, we document how multivariate statistics and magma differentiation modeling based on a large data set of glass compositions can be combined to constrain magma differentiation and plumbing system dynamics. Major and trace elements of matrix glasses erupted at Stromboli volcano (Italy) over the last 20 years provide a benchmark against which to test our integrated petrological approach. Principal component analysis, K-means cluster analysis, and kernel density estimation reveal that trace elements define a multivariate space whose eigenvectors are more readily interpretable in terms of petrological processes than major elements, leading to improved clustering solutions. Comparison between open- and closed-system differentiation models outlines that steady state magma compositions at constantly replenished and erupting magmatic systems approximate simple fractional crystallization trends, due to short magma residence times. Open-system magma evolution is associated with magma storage crystallinities that are lower than those associated with closed-system scenarios. Accordingly, open-system dynamics determine the efficient crystal-melt separation toward the top of the reservoir, where eruptible melts continuously supply the ordinary activity. Conversely, a mush-like environment constitutes the bottom of the reservoir, where poorly evolved magmas result from mixing events between mush residual melts and primitive magmas injected from deeper crustal levels.

Plain Language Summary Volcanoes characterized by continuous eruptive activity are typified by constant replenishment of new magma, rising from deeper regions of the crust. The volcanic glass (supercooled silicate melt), represents the residual liquid of magma crystallization, and is found as the intracrystalline matrix of eruptive products. The study of its chemical composition may provide insight into the processes occurring at depths beneath the volcanic vent, where magma compositional changes result from crystallization and mixing with new magma rising from depth. We combine statistical analyses and analytical equations based on the chemical composition of the matrix glasses from Stromboli volcano, in order to constrain the processes which produce their chemical variations, identifying different environments where magmas are stored at depth. Our results also show that when magma is stored for a short period of time, the chemical changes to which the magma is subjected in a constantly replenished system are similar to those occurring in a system which is closed to new inputs of magma.

Key Points:

- The combination of multivariate statistics with geochemical modeling provides new constraints on magma differentiation processes
- Multivariate statistics based on trace elements allow better retrieval of petrological information than those based on major elements
- Magma differentiation in open systems approximates that occurring in closed systems when magma residence timescales are short

Supporting Information:

Supporting Information may be found in the online version of this article.

Correspondence to:

A. Pontesilli,
alessio.pontesilli@ingv.it

Citation:

Pontesilli, A., Di Fiore, F., Scarlato, P., Ellis, B., Del Bello, E., Andronico, D., et al. (2024). Magma differentiation in dynamic mush domains from the perspective of multivariate statistics: Open- versus closed-system evolution. *Geochemistry, Geophysics, Geosystems*, *25*, e2023GC011396. https://doi.org/10.1029/2023GC011396

Received 15 DEC 2023
Accepted 9 FEB 2024

Author Contributions:

Conceptualization: A. Pontesilli
Data curation: A. Pontesilli
Funding acquisition: P. Scarlato, E. Del Bello

1. Introduction

Open-system magma dynamics typically characterize shallow crustal reservoirs that are constantly refilled by inputs of mafic magma over short temporal scales and where continuous magma ascent and degassing determine persistent volcanic activity (Edmonds et al., 2022). This volcanic regime characterizes several of the most hazardous volcanic areas worldwide, such as Fuego, Guatemala (Liu et al., 2020), Batu Tara, Indonesia (Spina et al., 2021), Mt. Etna, Italy (Di Renzo et al., 2019; Mollo et al., 2022), Cumbre Vieja, Spain (Di Fiore, Vona, Mollo, et al., 2023; Di Fiore, Vona, Scarani, et al., 2023; Taddeucci et al., 2023; Ubide et al., 2023). Quantitative

Investigation: A. Pontesilli, F. Di Fiore, B. Ellis, D. Andronico
Methodology: A. Pontesilli
Visualization: A. Pontesilli, F. Di Fiore
Writing – original draft: A. Pontesilli
Writing – review & editing: A. Pontesilli, F. Di Fiore, P. Scarlato, B. Ellis, E. Del Bello, D. Andronico, J. Taddeucci, M. Brenna, M. Nazzari, O. Bachmann, S. Mollo

modeling of magma differentiation in open-systems highlights that the liquid lines of descent substantially depart from standard fractional crystallization scenarios (Albarede, 1985; Lee et al., 2014; O'Hara, 1977; O'Hara & Mathews, 1981; O'Hara & Herzberg, 2002; O'Neill & Jenner, 2012). As a consequence, interpreting magmatic evolution and crystallization processes within open-systems is particularly challenging but crucial, because the steady state eruptive activity is punctuated by violent and threatening paroxysmal events, which are often related to the arrival of mafic magma in shallow storage zones (e.g., Petrone et al., 2022; Ubide & Kamber, 2018). A better definition of the geochemical evolution of such complex plumbing systems is also instrumental to petrological monitoring practices, as it provides the framework required to correctly interpret present and future eruptive scenarios (Blundy & Cashman, 2008; National Academy of Sciences, 2017).

Geochemical investigation of magmatic rocks classically involves bivariate representations of compositional data sets, where the concentrations of single elements (and/or their ratios) are plotted in two spatial dimensions, allowing the interpretation of magmatic processes at play as well as their magnitudes (e.g., Allègre & Minster, 1978; Rollinson, 1993). Diagrams where chemical analyses are normalized to a reference composition are also employed to simultaneously visualize multiple concentration patterns, but are less suited to represent large data sets because compositional trends could be obscured (Rollinson, 1993). Unlike these more traditional geochemical representations, multivariate statistics allows the treatment of large data sets and multiple elements at once, through the derivation of a reduced number of transformed variables, whilst retaining the petrological information contained therein (e.g., Davis, 2002; Joliffe, 2002; Le Maitre, 1982). Multivariate statistics have thus increasingly been adopted in magmatic petrology as, by virtue of the reduced dimensionality of transformed data sets, they provide convenient yet highly informative means of investigating geochemical data sets (e.g., Kuritani et al., 2016; Ragland et al., 1997; Thy & Esbensen, 1993; Ubide et al., 2014; Ueki & Iwamori, 2017; Zieg & Wallrich, 2018). However, their potential to successfully unfold the chief melt differentiation trends controlling the geochemical evolution of a volcanic system is yet to be unlocked.

Stromboli volcano in Italy represents an ideal case study to test the potential of multivariate statistics to disentangle magmatic processes determining melt differentiation, as the compositional spectrum of erupted products is routinely documented (e.g., Bragagni et al., 2014; Di Stefano et al., 2020; Francalanci et al., 1989, 1999, 2012; Landi et al., 2004, 2022; Petrone et al., 2022; Pontesilli et al., 2023; Schiavon et al., 2023). The Present-Day (<1.5 ky; Bertagnini et al., 2011; Francalanci et al., 2013; Rosi et al., 2000) activity at Stromboli is closely associated with two main magma types, emitted as low-porphyritic pumices (*lp*, crystallinity <10 vol%, mostly olivine and clinopyroxene) and high-porphyritic scoriae (*hp*, crystallinity ∼50 vol%, of which 30–35 vol% plagioclase) (e.g., Francalanci et al., 2004, 2013; Landi et al., 2004). The bulk compositions of *lp* pumices and *hp* scoriae closely resemble those of *lp* matrix glasses, showing a tendency to cluster at high-K to shoshonitic basalts (49.2–51 wt.% SiO_2, 1.7–2.4 wt.% K_2O, 5.6–6.7 wt.% MgO, and 10.5–12.1 wt.% CaO; e.g., Francalanci et al., 2004; Petrone et al., 2022). The compositions of *hp* matrix glasses, however, are in the range of shoshonites (51.1–54.5 wt.% SiO_2, 3.5–5.2 wt.% K_2O, 3–4.1 wt.% MgO, and 6.1–8.3 wt.% CaO; e.g., Francalanci et al., 1999, 2013; La Felice & Landi, 2011; Landi et al., 2004). Matrix glasses with compositions intermediate between *hp* and *lp* melts, often characterized by mixing/mingling textures, have also been reported (49.8–53.3 wt.% SiO_2, 2.3–3.7 wt.% K_2O, 3.9–5.8 wt.% MgO, and 7.8–10.6 wt.% CaO; Andronico et al., 2008; Landi et al., 2008, 2022). The ordinary eruptive activity at Stromboli taps differentiated *hp* magmas stored in a shallow reservoir ($P < 100$ MPa) and is characterized by low energy explosions with volumes of erupted products on the order of 1–10 m^3 (Rosi et al., 2013). Conversely, the more violent activity is fed by mafic *lp* magmas rising from deeper storage levels ($P > 190$ MPa) and is associated with "major" and paroxysmal eruptions with volumes of erupted products on the order of 10^4 m^3 (Andronico et al., 2021; Di Stefano et al., 2020; Francalanci et al., 2004; Metrich et al., 2001; Petrone et al., 2022). Major eruptions do not affect the settled areas but only the upper part of the volcano, whereas paroxysms are a threat to the inhabitants and villages because of their higher eruptive volumes (Barberi et al., 1993). Both major eruptions and paroxysms may also contain intermediate matrix glasses, generally interpreted as melts from a transitional storage area located between the shallower and the deeper reservoirs (Landi et al., 2008, 2022). Moreover, subtle chemical and thermal gradients in the *hp* reservoir are responsible for compositional heterogeneities in the products of the ordinary activity of Stromboli (Pontesilli et al., 2023).

In this study, we employ a statistical and geochemical modeling approach on a suite of matrix glass representative of primitive melts to differentiate melts from normal, major and paroxysmal eruptions that occurred at Stromboli over the last 20 years. A new extensive geochemical data set has been compiled for 24 eruptions, comprising

1,365 major oxide and 984 trace element data points collected using the same analytical facilities in order to eliminate, or minimize as far as possible, the source of uncertainties inherent in interlaboratory comparisons. The data set was interrogated by principal component analysis (PCA), K-means cluster analysis (KCA) and kernel density estimation (KDE) conducted on log-ratio transformed data. Magmatic processes responsible for the clustering of melt compositions in the principal component space are quantified by iterative solutions of open- and closed-system geochemical modeling equations. This multifaceted approach shows that multivariate statistics are a convenient and effective means to probe large analytical data sets and unfold subtle magma compositional changes, and hence provide unbiased constraints on the plumbing system architecture and magma dynamics of active basaltic volcanoes.

2. Methods

2.1. Analytical Methods

Major oxide analyses were carried out at the HP-HT Laboratory of Experimental Volcanology and Geophysics of the Istituto Nazionale di Geofisica e Vulcanologia (INGV) in Rome, Italy, with a Jeol-JXA8200 electron probe micro-analyzer (EPMA) equipped with five spectrometers. A beam size of 10 μm was used, by applying a counting time of 5 s on background and 15 s on peak. Corrections for inter-elemental effects were made using a ZAF (Z, atomic number; A, absorption; F, fluorescence) procedure. The following calibration standards were adopted from Micro-Analysis Consultants (MAC; http://www.macstandards.co.uk): albite (Si-PET, Al-TAP, Na-TAP), forsterite (Mg-TAP), augite (Fe-LIF), apatite (Ca-PET, P-PET), orthoclase (K-PET), rutile (Ti-PET) and rhodonite (Mn-LIF). Sodium and potassium were analyzed first to minimize alkali migration effects. The accuracy and precision of microprobe data was estimated through the analysis of well-characterized minerals as unknowns and is reported in Supporting Information S1. Based on the analysis of secondary standards, analytical uncertainties relative to their reported concentrations indicated that precision was better than 5% for all cations except for Na (~7%) and Mn (~10%). Backscattered electron (BSE) images were collected with a field emission gun-scanning electron microscopy (FEG-SEM) Jeol 6500F equipped with an energy-dispersive spectrometer (EDS) detector, also installed at the HP-HT Laboratory at INGV.

Trace element analyses were conducted at the Institute of Geochemistry and Petrology of the ETH Zürich (Switzerland) by using a 193 nm excimer laser coupled with second generation two-volume constant geometry ablation cell (Resonetics S-155LR) and a high-sensitivity, sector-field inductively coupled plasma mass spectrometer (ICP-MS; Thermo:Element XR). Points with a spot size of 43 μm were set on optically homogeneous portions of the material previously analyzed by EPMA and were ablated with a pulse rate of 10 Hz and an energy density of 3.5 J/cm^2 for 40 s. Ablated material was extracted in a stream of He (500 mL/min) and then mixed with Ar (1 L/min) and N_2 (2 mL/min) before entering the plasma. Isotopes were analyzed relative to an internal standard of known composition (i.e., NIST612). A second reference material (i.e., GSD-1G) was used as an unknown to check data quality during each analytical run. ^{29}Si and ^{43}Ca were used as internal standards. Precision estimates based on GSD-1G reference material varied depending upon several factors (e.g., the element and isotope analyzed, as well as the homogeneity of the ablated material) but was typically less than 6% for most trace elements, except for Ni (~7%) and Th (~13%). Accuracy estimates indicate that on the average analytical results are within 5% of reference values. Accuracy and precision estimates based on the secondary standard are fully reported in Supporting Information S1. Long-term performance based on repeated analyses over the past 8 years indicates that trace element reproducibility is on the order of ~6% (cf. Ellis et al., 2022) and in good agreement with GeoReM preferred values (Jochum et al., 2005).

A complete list of analyzed samples, including eruption date for each sample, is reported in Table S1 in Supporting Information S1. In conducting major and trace element analyses, only microlite-poor glasses were considered (less than 5 vol% microlites; cf. Pontesilli et al., 2023).

2.2. Statistical Approach

PCA is a well-established procedure in statistics to reduce the dimensionality of a multivariate data set while retaining the original amount of variance contained therein. It relies on the linear combination of a certain number of measured variables, and the optimization of their variance distribution. Inherent correlations in the original data set are thus transformed into a new set of orthogonal vectors, typically representing the eigenvectors of the correlation matrix (e.g., Le Maitre, 1982). Accordingly, PCA employs a rigid rotation of axes, which results in

transforming the original set of variables into principal components (from PC1 to PCk, where k represents the number of original variables), which are uncorrelated between each other (orthogonal; Joliffe, 2002). PCA optimizes variance distribution, where PC1 collects most of the variance, whereas decreasing variance is assigned to each subsequent PCk. This is illustrated in the so-called Scree plots, corresponding to histograms of variance distribution across principal components. Recasting the data through PCA provides some important benefits: (a) it allows for an optimal visualization of data since the largest part of the variance in the original data set is now expressed by a smaller number of variables, (b) it reduces the number of dimensions required to describe the data, accounting for intrinsic correlations between variables, as for instance among major or trace elements with a similar geochemical behavior, (c) it constitutes an unbiased method since it involves neither assumptions about the original variables, nor hypotheses or models to be tested (Marriott, 1974). In synthesis, PCA provides a more convenient means of expressing and interpreting the input data set, especially when principal components can be interpreted in terms of the underlying processes which are producing such variations in the original data set, a procedure known as "reification" (e.g., Davis, 2002; Joliffe, 2002). Reification can be performed by inspecting the loadings, which range between −1 and 1, and represent the contribution of each original variable on the transformed variables. Once at least a principal component has been robustly interpreted, the other principal components may be explored by investigating the existing relationships between their scores. Therefore, reification represents a crucial step in PCA, as it requires the most care and deep understanding of the underlying data (Davis, 2002).

In performing PCA, we avoid any potential spurious correlation between variables of the investigated data sets by processing data through a log transformation followed by standardization. This procedure aims at minimizing closure effects, which affect compositional data totaling a fixed sum (e.g., major element oxides totaling 100 in wt %; Aitchison, 1999; Davis, 2002). The natural logarithm of the major oxide data is then standardized using the z-score, hence subtracting the mean and dividing by the standard deviation of the log-transformed input. To compare the results of multivariate analyses performed on major and trace elements, log-transformation is also applied to trace element data. Then, λ_j eigenvalues and v_j eigenvectors are extracted from a symmetrical $m \times m$ matrix of elements $a_{i,j}$ called A, defined as

$$A\, v_j = \lambda_j\, v_j \tag{1}$$

A is the correlation matrix for the original variables. The principal component score z_{ij} represents the coordinates of the ith original data point x_{ik}. Once projected onto the transformed PC space, z_{ij} is calculated as (Le Maitre, 1982):

$$z_{ij} = \sum_{j=1}^{m} v_{jk} \frac{x_{ik} - \overline{x_k}}{\sigma_{xk}} \tag{2}$$

where $\overline{x_k}$ is the mean value of the kth variable and σ_{xk} represents its standard deviation. In order to identify compositional groups in the transformed data sets for major and trace elements, we employ KCA of principal component scores. This approach follows the principle that PCA dimension reduction provides the best low-dimensional linear approximation of data to perform data clustering according to the K-means objective function (Ding & He, 2004). In KCA, the data set is iteratively grouped into K clusters by assigning each data point to one of the randomly selected initial cluster centroids. Cluster centroids are then recalculated as to progressively decrease the total Euclidean distance between all data points and each κth cluster, as calculated by the K-means objective function that is expressed by error minimization:

$$J_K = \sum_{\kappa=1}^{K} \sum_{i=1} (z_i - c_\kappa)^2 \tag{3}$$

where z_i is the ith data point expressed as the principal component score (as above) and c_κ represents the centroid of the κth cluster. For each K, minimization of the function J_K expressed by Equation 3 allows to determine the optimal κth cluster to which each data point is assigned. This iterative procedure is repeated for an increasing number K of initial cluster seeds, and the optimal solution is then chosen based on the inertia for each clustering solution, which is represented by the sum of all Euclidean distances for a given K and the average Euclidean

distance across clusters (Everitt et al., 2011). The best fit clustering solution is then based on the knee principle, by identifying the value of K, which corresponds to a break in the slope of decreasing inertia with increasing K (Figure S1 in Supporting Information S1; Everitt et al., 2011).

Probability density functions are employed to better compare variables for each cluster of the data set. For this purpose, we used KDE, which is a non-parametric method for estimating the probability distribution of a random variable based on a random sample, adopting a Gaussian kernel and estimating the optimum bandwidth via the criteria described by Silverman (1986). Calculations of PCA, KCA, and KDE presented in this work were performed using the Real Statistics Resource Pack software® (Copyright 2013–2022: Zaiontz (2022); www.real-statistics.com; Release 8.0).

2.3. Petrological Modeling

Interpretation of geochemical data in magmatic systems is largely based on modeling the compositional variability of rock suites by means of analytical equations designed to quantify the geochemical consequences of the main magma differentiation processes (e.g., Allègre & Minster, 1978; O'Hara & Herzberg, 2002; Rollinson, 1993). The simplest case of such geochemical equations is represented by fractional crystallization in a closed-system, which may be modeled by means of the Rayleigh Fractional Crystallization equation (hereafter, FC):

$$C_L = C_0\,(1-x)^{D-1} \tag{4}$$

where C_L and C_0 represent the concentrations of the element of interest in the derivative and parental liquids, respectively. x represents the fraction of material crystallized and D represents the bulk partition coefficient:

$$D_k = \sum\nolimits_p w_p\, D_{k,p} \tag{5}$$

w_p is the weight fraction of the pth mineral phase and $D_{k,p}$ is the partition coefficient for the kth element of interest. A comprehensive $D_{k,p}$ list from partitioning studies on basaltic magmas is included in Table S4 in Supporting Information S1. Equation 4 was slightly modified by Langmuir (1989) to account for a portion of the liquid evolving not in the main reservoir, but in the more crystalline margins of the chamber before being returned to it (e.g., Di Stefano et al., 2020; Pontesilli et al., 2022):

$$C_L = C_0\,(1-x)^{f(D-1)/[D(1-f)+f]} \tag{6}$$

where the parameter f is the fraction of material which is still liquid in the chamber margins at the time it returns to the main reservoir. f ranges between 0, in case of complete solidification of the chamber margins with no differentiation effect in the main reservoir, and 1 if all the material in the chamber margins returns to the main reservoir. In the latter case, Equation 6 reduces to the simple case for FC, as reported in Equation 4.

On the other hand, magma differentiation occurring in open-systems diverges from closed-system scenarios, by the effect of periodic injections of more mafic parental magma and continuous tapping of the reservoir. Such open-system dynamics may impart distinctive geochemical trends to the liquid lines of descent of magmas from different tectonic settings, such as mid-ocean ridges and arcs (Albarede, 1985; Lee et al., 2014; O'Hara, 1977; O'Hara & Mathews, 1981; O'Neill & Jenner, 2012). O'Hara and Mathews (1981) proposed an equation for constantly recharged, mixed, crystallized before tapped magma chambers (RMXTC; O'Hara & Herzberg, 2002):

$$C_{L_{n+1}} = \frac{(1-x_q)^{D_q-1}}{M_{n+1}}\left[M_0\prod\nolimits_{q=0}^{q=n}(1-x_q-y_q)(1-x_q)^{D_q-1} + \sum_{q=0}^{q=n} C_{z_q} z_0\,\frac{\prod_{q=0}^{q=n}(1-x_q-y_q)(1-x_q)^{D_q-1}}{\prod_{q=0}^{q=q}(1-x_q-y_q)(1-x_q)^{D_q-1}}\right] \tag{7}$$

where x and D are again the fraction of material crystallized and the bulk partition coefficient, respectively, while y is the amount of material erupted, at each cycle q comprised between 0 and n. $C_{L_{n+1}}$ represents the composition of

the erupted liquid at the end of the $n+1$th cycle. By assuming constant mass of the magma reservoir ($M_0 = M_{n+1}$), x, y, D, and a constant composition for the recharging magma, the composition of the steady state liquid $C_{L_{ss}}$ after a certain number of differentiation cycles is (O'Hara, 1977; O'Hara & Mathews, 1981):

$$C_{L_{ss}} = C_0 \frac{(x+y)(1-x)^{D-1}}{1-(1-x-y)(1-x)^{D-1}} \tag{8}$$

Because Equation 7 is derived by assuming melt evolution according to FC (Equation 4), at the end of each $n+1$th cycle, the composition of the residual liquid is

$$C_{L_{n+1}} = C_{M_{n+1}} (1-x)^{D-1} \tag{9a}$$

$C_{M_{n+1}}$ is the bulk composition of the magma chamber at the $n+1$th cycle. The bulk composition of the crystallized material ($C_{S_{n+1}}$) is calculated by mass balance arguments as follows:

$$C_{M_{n+1}} = x\, C_{S_{n+1}} + (1-x)\, C_{L_{n+1}}$$

$$x\, C_{S_{n+1}} = C_{M_{n+1}} - (1-x)^{D-1}(1-x)\, C_{M_{n+1}}$$

$$C_{S_{n+1}} = C_{M_{n+1}} \frac{1-(1-x)^{D}}{x} \tag{9b}$$

In analogy with Equation 9a, the exponent in Equation 6 accounts for the effect of in situ crystallization at the chamber's margin during each nth cycle, by introducing the parameter f (Langmuir, 1989):

$$C_{L_{n+1}} = C_{L_n} (1-x)^{f(D-1)/[D(1-f)+f]} \tag{10a}$$

and the bulk composition of the crystallized material is derived as described above (Equation 9b):

$$C_{M_{n+1}} = x\, C_{S_{n+1}} + (1-x)\, C_{L_{n+1}}$$

$$x\, C_{S_{n+1}} = C_{M_{n+1}} + (1-x)^{f(D-1)/[D(1-f)+f]}(1-x)\, C_{M_{n+1}}$$

$$C_{S_{n+1}} = C_{M_{n+1}} \frac{1-(1-x)^{D/[D(1-f)+f]}}{x} \tag{10b}$$

Accordingly, Equation 8 becomes

$$C_{L_{ss}} = C_0 \frac{(x+y)(1-x)^{f(D-1)/[(D(1-f)+f]}}{1-(1-x-y)(1-x)^{f(D-1)/[D(1-f)+f]}} \tag{11}$$

Equations 8 and 11 apply when eruption occurs after magma recharge, mixing and subsequent fractionation at each cycle (RMXTC), and $C_{L_{n+1}}$ approaches the steady state composition $C_{L_{ss}}$. As pointed out by Albarede (1985), if eruption follows magma recharge and mixing, but precedes fractionation (recharged, mixed before tapped, crystallized magma chambers; RMTXC; O'Hara & Herzberg, 2002), then the composition of the liquid at each $n+1$th differentiation cycle is now that of the liquid after mixing ($C_{M_{n+1}}$). This can be calculated by mass balance, since we assume no change in the mass of the magma reservoir:

$$(x+y)\, C_0 = x\, C_{S_{n+1}} + y\, C_{M_{n+1}} \tag{12a}$$

and by substituting Equation 9b into Equation 12a:

$$(x+y)\, C_0 = x\, C_{M_{n+1}} \frac{1-(1-x)^{D}}{x} + y\, C_{M_{n+1}} \tag{12b}$$

Under steady state conditions, Equation 12b becomes

$$C_{L_{ss}} = C_{M_{n+1}} = C_0 \frac{(x+y)}{1+y-(1-x)^D} \tag{12c}$$

the exponent is now the same as in Equation 9b. By considering the in situ crystallization effects during open-system evolution, the exponent corresponds to that of Equation 10b:

$$C_{L_{ss}} = C_0 \frac{(x+y)}{1+y-(1-x)^{D/[D(1-f)+f]}} \tag{13}$$

Our modeling approach is based on Equation 6 to track a closed-system differentiation. Equations 11 and 13 are used to model open-system differentiation for *hp* and intermediate magma compositions, respectively. Calculations are performed iteratively for each data point, through a Monte Carlo procedure by randomly varying the equation parameters (x, y, f, mineral relative proportions) as to minimize the root mean square error (RMSE) between modeled and observed principal component scores. Calculations start either from parental melt compositions C_0 or from the derivative liquid compositions $C_{L_{ss}}$. *lp* matrix glass compositions are considered as parental melts, representing the most primitive compositions erupting during the Present-Day activity, also closely resembling *lp* pumice whole-rocks (e.g., Di Stefano et al., 2020; Métrich et al., 2001, 2010; Petrone et al., 2022). Derivative melts are represented by *hp* and intermediate matrix glasses, resulting from variable degrees of magma differentiation and mixing within the plumbing system (e.g., Francalanci et al., 1989, 2013; Landi et al., 2008, 2022). Each calculated melt composition is compared with matrix glass compositions randomly varied at each iteration in a range comprised between two standard deviations below and above the average composition, as to avoid any bias in the calculations related to the assumption of a fixed composition to which modeled melt compositions are compared. Calculations are performed on the basis of principal component scores for each data point. The fitting procedure is based on the variance-covariance structure instead of absolute elemental abundances, in order to maximize the representativeness of modeling results. To ensure that the principal component scores for the modeled data set are consistent with the scores of the initial data set, they are standardized with the means and standard deviations of the log-transformed elemental concentrations from the initial data set and projected onto the same eigenvectors, according to Equation 2.

3. Results

3.1. Multivariate Statistics of Major and Trace Elements

The input data set comprises 10 major elements expressed as oxide components (SiO_2, TiO_2, Al_2O_3, FeO, MnO, MgO, CaO, Na_2O, K_2O, and P_2O_5) and 32 trace elements (Li, Sc, V, Cr, Co, Ni, Rb, Sr, Y, Zr, Nb, Cs, Ba, La, Ce, Pr, Nd, Sm, Eu, Gd, Tb, Dy, Ho, Er, Tm, Yb, Lu, Hf, Ta, Pb, Th, U) from Stromboli's matrix glasses. PCA generates principal components (PC) equal to the number of major (from $PC1_{ME}$ to $PC10_{ME}$) and trace (from $PC1_{TE}$ to $PC32_{TE}$) elements (Figure 1). Eigenvalues, eigenvectors, and system variance for each principal component (together with the correlation matrix of the data set) are listed in Tables S2 and S3 in Supporting Information S1 for major and trace elements, respectively. PC_{ME} and PC_{TE} account for unique linear combinations of the input variables expressed by the eigenvectors of their respective correlation matrices. The system variance decreases with an increase in the number of principal components, but this trend is less pronounced for major elements (Figure 1a) than for trace elements (Figure 1b).

For major elements, $PC1_{ME}$ describes 76% of the total variance (Figure 1a), displaying positive loadings for SiO_2, TiO_2, MnO, FeO, Na_2O, K_2O, and P_2O_5, with a minor contribution of MnO (Figure 1c). Negative loadings on $PC1_{ME}$ account for Al_2O_3, MgO, and CaO (Figure 1c). The remaining system variance is expressed by $PC2_{ME}$ (9.5%), $PC3_{ME}$ (5.6%), and $PC4_{ME}$ (3.6%). The dimensionality of $PC2_{ME}$ and $PC3_{ME}$ is chiefly controlled by MnO and Na_2O, respectively. Loadings on $PC4_{ME}$ are always lower than 0.4 (Figure 1c).

For trace elements, $PC1_{TE}$ describes 86.3% of system variance, whereas $PC2_{TE}$ (4.5%), $PC3_{TE}$ (2.8%) and $PC4_{TE}$ (1.3%) represent a minor contribution to the data set variance (Figure 1b). Loadings on $PC1_{TE}$ are high (>0.9 or <-0.6) for all trace elements, except for Li (<0.4). For Sc, Cr, Co, Ni, and Sr, $PC1_{TE}$ and $PC2_{TE}$ show negative and positive loadings, respectively (Figure 1d). Along $PC1_{TE}$, these loadings are anticorrelated with the largest

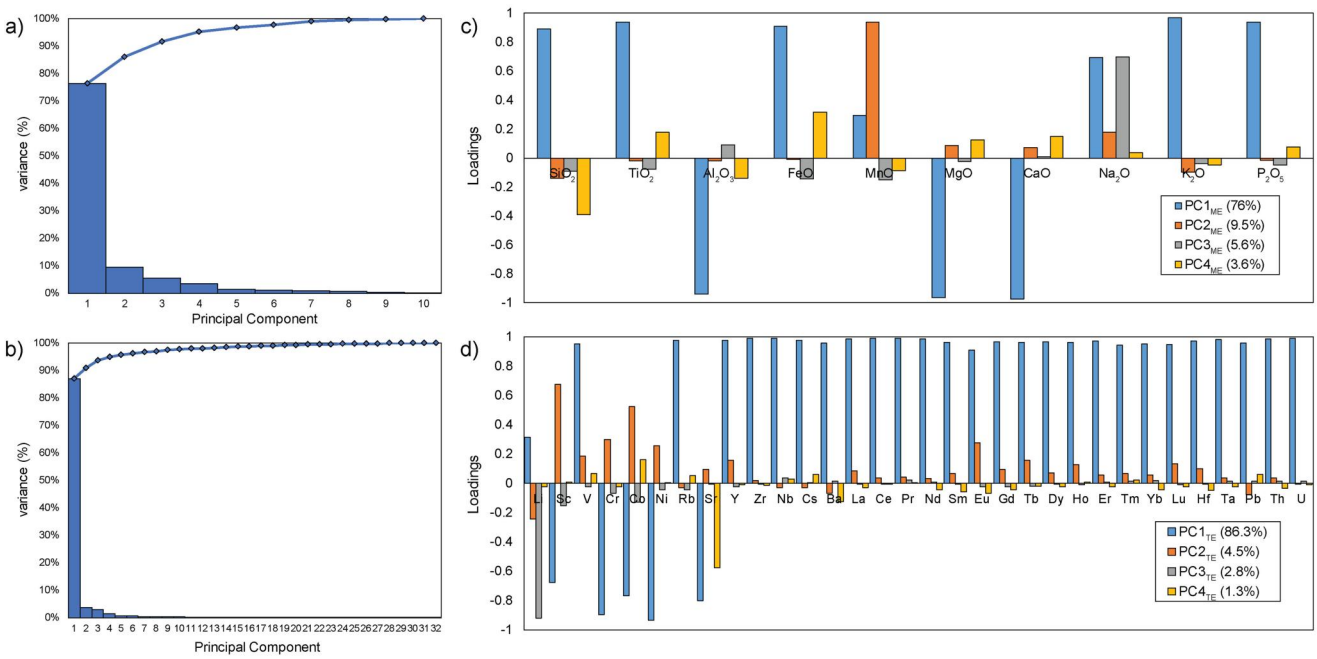

Figure 1. Results of PCA carried out on matrix glass compositions. Scree plots show the decrease in variance (in blue) bars for the principal components of 10 major oxides (a) and 32 trace elements (b) assumed as the system variables. The cumulative variance is also plotted as blue diamonds connected by a solid line. Loadings of major oxides on $PC1_{ME}$, $PC2_{ME}$, $PC3_{ME}$, and $PC4_{ME}$ (c) and of trace elements on $PC1_{TE}$, $PC2_{TE}$, $PC3_{TE}$, and $PC4_{TE}$ (d) are also shown.

group of trace elements (Li, V, Rb, Pb, rare earth elements, high field strength elements, and actinides), whereas they show negligible loadings on $PC2_{TE}$ (Figure 1d). Most of the dimensionality of $PC3_{TE}$ and $PC4_{TE}$ is represented by the negative loadings for Li and Sr, respectively (Figure 1d).

In accordance with the inertia criteria and visual inspection (Figure S1 in Supporting Information S1), the best fit number of clusters in the 10-dimensional Euclidean space is found at three for major elements (i.e., 1_{ME}, 2_{ME}, 3_{ME}), and at four for trace elements (i.e., 1_{TE}, 2_{TE}, 3_{TE}, and 4_{TE}). Centroid coordinates are reported in Tables S1 and S2 in Supporting Information S1 for major and trace elements, respectively. Euclidean distances and cluster assignment of each data point to the respective clusters are reported in Supporting Information S1. Clustering results are presented as major element bivariate plots for K_2O versus CaO (Figure 2) and TiO_2 versus Al_2O_3 (Figure S2 in Supporting Information S1), and trace element bivariate plots for Zr versus Ni (Figure 3) and Cr versus Rb (Figure S3 in Supporting Information S1). These plots also show principal component scores derived for $PC1_{ME}$-$PC2_{ME}$ and $PC1_{TE}$-$PC2_{TE}$, together with probability density functions from KDE. Cluster assignments for $PC1_{ME}$-$PC3_{ME}$, $PC1_{ME}$-$PC4_{ME}$, $PC1_{TE}$-$PC3_{TE}$ and $PC1_{TE}$-$PC4_{TE}$ scores are illustrated in Figure 4. Probability density functions for $PC3_{ME}$, $PC4_{ME}$, $PC3_{TE}$ and $PC4_{TE}$ are also displayed in Figure S4 in Supporting Information S1.

Clusters 1_{ME}, 2_{ME}, and 3_{ME} closely overlap with the analyses of matrix glasses from literature, referring to the compositions of *lp*, intermediate, and *hp* magmas, respectively (Figures S5a and S5b in Supporting Information S1). Similarly, clusters 1_{TE} and 2_{TE} resemble the analytical ranges of *lp* and intermediate matrix glasses, respectively (Figures S5c and S5d in Supporting Information S1). A more complex pattern is seen in the $PC1_{TE}$-$PC2_{TE}$ space where the *hp* matrix glasses can be subdivided into cluster 3_{TE} and cluster 4_{TE} (Figures S5c and S5d in Supporting Information S1). This latter is characterized by lower $PC1_{TE}$ and $PC2_{TE}$ scores (Figure 3), and higher $PC3_{TE}$ scores (Figure 4).

3.2. Open- Versus Closed-System Magma Differentiation

Modeling predictions, based on the iterative solution of geochemical equations allow unbiased comparison of results from the open- and closed-system magma differentiation at Stromboli. In Figure S6 in Supporting Information S1, probability density distributions of principal component scores for the original data are

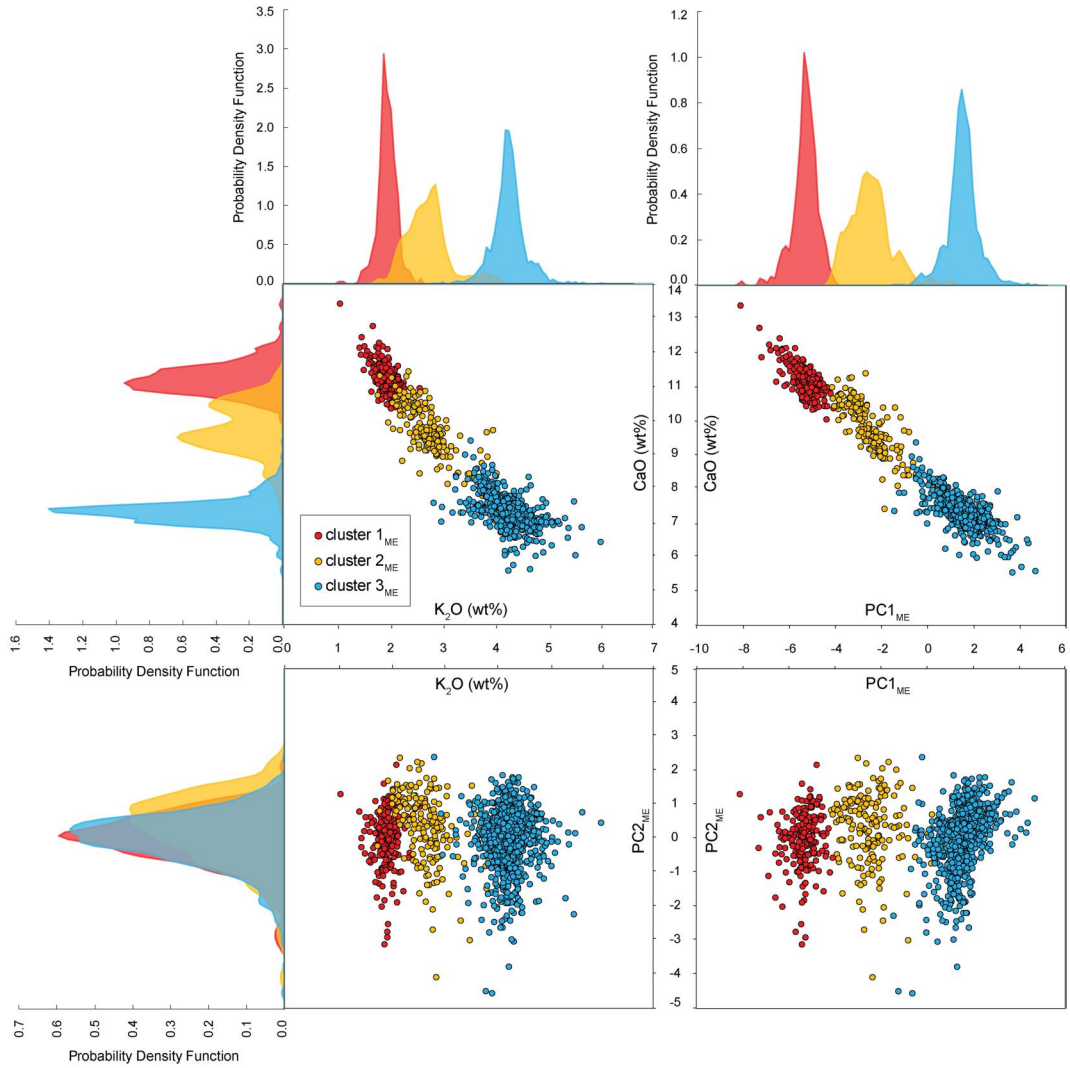

Figure 2. Bivariate plots of CaO against K_2O (in wt%) and principal component scores based on major elements (i.e., $PC1_{ME}$ and $PC2_{ME}$) integrated with kernel density estimates for each cluster.

juxtaposed to modeling results, showing that both open- and closed-system processes reproduce well the matrix glass compositions (see the low values of RMSE in Figure S7 in Supporting Information S1). The main equation parameters refined using this method are reported in Figure 5 where open-and closed-system modeling results are compared. The mineral relative proportions are plotted in Figure S8 in Supporting Information S1, whereas the parameters y and z are plotted in Figure S9 in Supporting Information S1. The fraction of crystallized material x plotted in Figure 5 represents the parameter diverging the most between open- and closed-system scenarios. As a consequence, the magnitude of x fundamentally controls the differentiation trends plotted in Figure 6, when all other parameters are kept constant at best case modal values, determined by probability density functions (Figure 5). However, by keeping constant the value of x and reiterating magma differentiation models over the entire range of modeling parameters (i.e., y, f, starting melt composition, and mineral relative proportions), the intrinsic variability of matrix glass compositions is also reproduced. In Figure 6, modeled differentiation trends depart, for illustrative purposes, from a single cluster 1_{TE} composition representing an *lp* composition from the 15 March 2007 paroxysm, whose principal component scores approximate the mean value of cluster 1_{TE} scores. For the modeling of trace elements, we adopt partition coefficients from the literature reported in Table S4 in Supporting Information S1. Adopted values for partition coefficients were based on literature values and apparent partition coefficients between natural mineral phases and glasses from Stromboli eruptive products (Petrone et al., 2022; Pontesilli

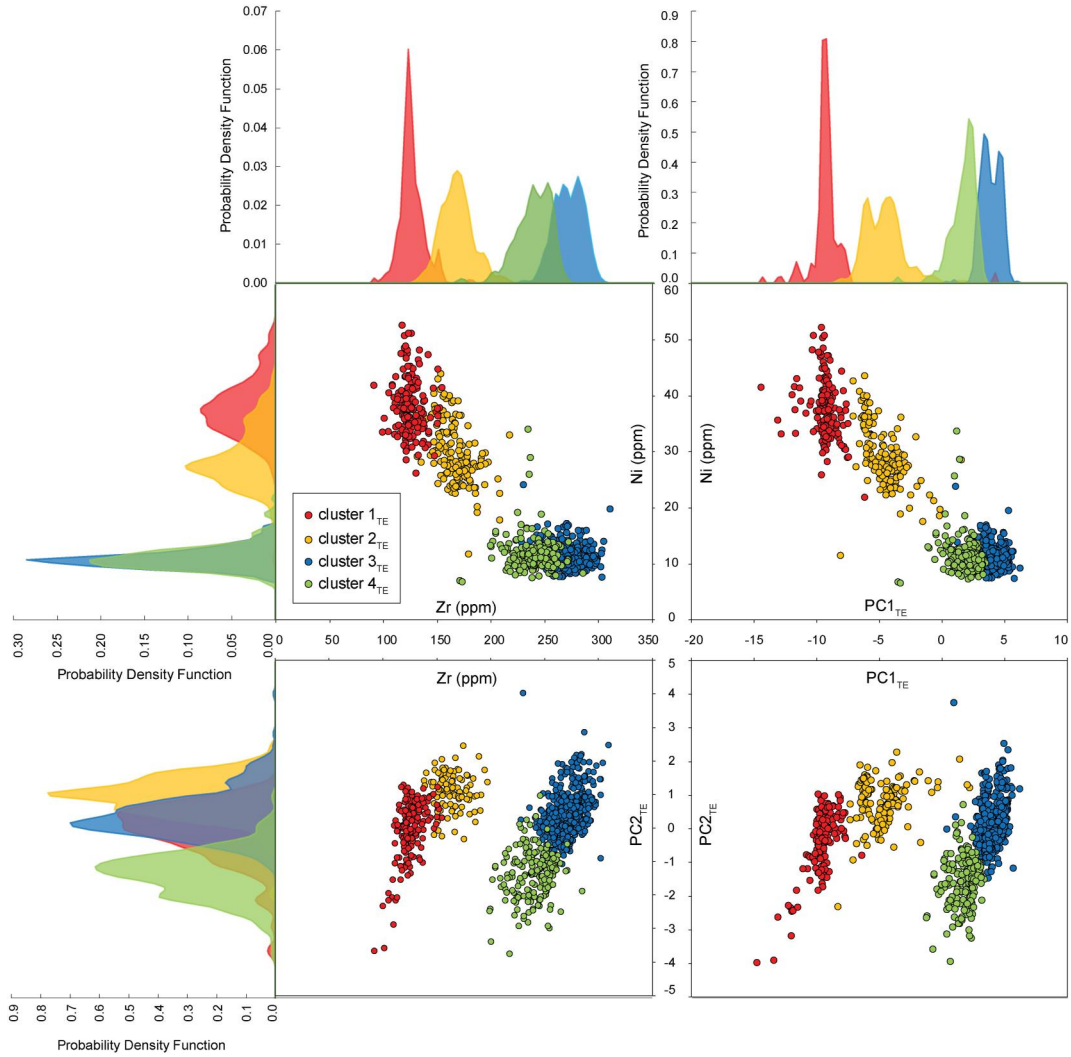

Figure 3. Bivariate plots of Ni against Zr (in ppm) and principal component scores based on trace elements (i.e., $PC1_{TE}$ and $PC2_{TE}$) integrated with kernel density estimates for each cluster.

et al., 2023; Table S4 in Supporting Information S1). To safeguard our modeling results against mistakenly chosen partition coefficients, their values are varied for an increasing number of randomly selected trace elements. Moreover, possible bias in the screening of partitioning coefficients from literature is prevented by using values over a broad range of physicochemical conditions (0.1–3,500 MPa, 1,000–1,350°C, and fO_2 between air and QFM-2; Supporting Information S1). Because $PC1_{TE}$ accounts for more than 86% of the trace elements variance (Figure 1c), error in $PC1_{TE}$ is modeled by averaging 100 random selections of one to five partition coefficients. As the number of randomly varied partition coefficients increases, the modal error resulting from open- and closed-system modeling increases from ≤0.5% to ≤2%, and the overall error range is always ≤5% (Figure S10 in Supporting Information S1).

Modeling results show that melt differentiation in the closed-system follows FC1, FC2 and FC3 trends, which are based on Equation 6 and intersect compositions belonging to clusters 3_{TE}, 4_{TE}, and 2_{TE}, respectively (Figure 6a). FC1 and FC2 trends, intersecting clusters 3_{TE} and 4_{TE}, respectively, are reproduced by fractionation of mineral assemblage consistent with phenocryst modal proportions observed in *hp* magmas at 40%–55% degree of crystallization (cf. Francalanci et al., 2012; Landi et al., 2004; Pontesilli et al., 2023). The angular coefficients of FC trends for clusters 3_{TE} and 4_{TE} are constrained by the parameter *f* estimated at 0.8–0.9 (Figure 5a). Conversely, cluster 2_{TE} is characterized by higher $PC2_{TE}/PC1_{TE}$ ratios, reflecting a crystallizing phase assemblage dominated by clinopyroxene and olivine, consistent with Landi et al. (2022),

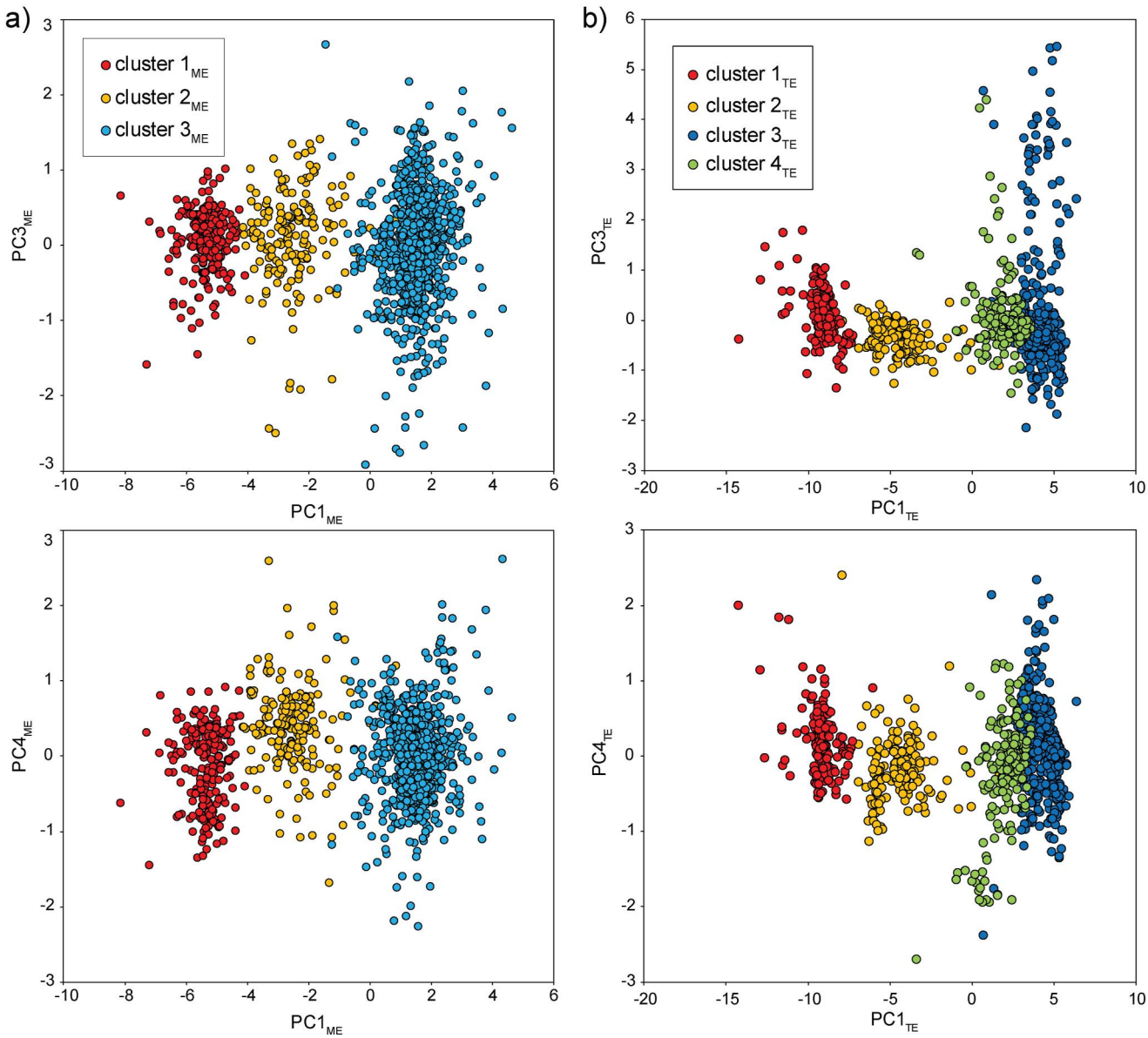

Figure 4. Bivariate plots of $PC1_{ME}$-$PC3_{ME}$ and $PC1_{ME}$-$PC4_{ME}$ scores based on major elements (a), and $PC1_{TE}$-$PC3_{TE}$ and $PC1_{TE}$-$PC4_{TE}$ scores based on trace elements (b).

which related these intermediate melt compositions to crystal fractionation processes dominated by mafic phases. Lower f values of ~0.25 (Figure 5a) indicate that in situ crystallization prevails over crystal fractionation for cluster 2_{TE}.

These results show that FC equations are overall successful in reproducing intermediate to more evolved magma compositions. However, open-system dynamics have been shown to control the textural evolution of *hp* products (Armienti et al., 2007) and the variable crystallization state of magma, as preserved in zoned crystals (Moschini et al., 2023; Petrone et al., 2022). In this scenario, closed-system models may represent a simplistic conceptualization of the plumbing system at Stromboli, as repeated *lp* magma inputs feed the persistent volcanic activity (e.g., Francalanci et al., 1989; Landi et al., 2004). The Present-day activity is also characterized by a remarkable compositional homogeneity of the eruptive products during the last 1500 years BP (Bertagnini et al., 2011; Rosi et al., 2000), suggesting that a condition of steady state is attained over time (O'Hara & Mathews, 1981). Therefore, we employ the modeling approach developed for constantly refilled,

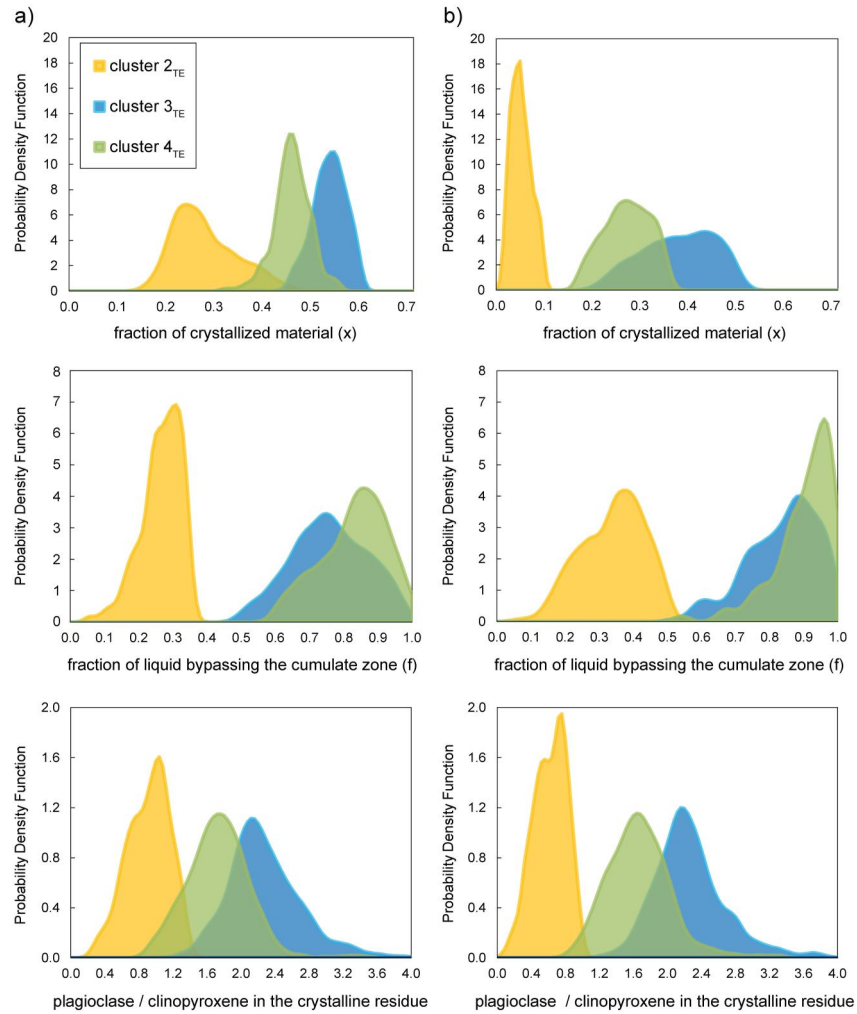

Figure 5. Kernel density estimates for the fraction of material crystallized (x), the fraction of liquid not involved in the cumulate zone (f), and the ratio between plagioclase and clinopyroxene in the fractionating phase assemblages estimated on the basis of Monte Carlo simulations for the closed-system case (a), and the open-system case (b). See Methods for further details on the modeling approach.

mixed, crystallizing, and erupting magma chambers to constrain the open-system evolution (Albarede, 1985; O'Hara, 1977; O'Hara & Mathews, 1981; O'Hara & Herzberg, 2002; O'Neill & Jenner, 2012; Lee et al., 2014; see Section 2 for further details). In particular, Equation 11 is adopted for our purposes by assuming that the mixing and fractionation precede eruption at each cycle (i.e., RMXTC trends in Figure 6b). The resulting RMXTC1 and RMXTC2 trends well reproduce the highly differentiated and degassed *hp* magmas belonging to clusters 3_{TE} and 4_{TE}, respectively, mostly by varying the degree of crystallization and, more specifically, the amount of plagioclase crystallized (Figure 6b). Indeed, compositional variability within the *hp* reservoir may be reproduced by increasing the degree of plagioclase fractionation (Figure S11 in Supporting Information S1).

On the other hand, the eruption of intermediate magmas (cluster 2_{TE}) is restricted to a few paroxysms and major eruptions, involving various degrees of interaction between the *lp* recharge and the *hp* reservoir (Landi et al., 2022). For these matrix glass compositions, Equation 13 is employed by considering that each eruption follows the *lp-hp* mixing process but precedes crystal fractionation (RMTXC). Best-fitting values for parameters used in open-system models are displayed in Figure 5b. It is important here to recall that, with respect to closed-system FC models, the parameters used for open-system modeling (Figures 5 and 6) correspond to averaged values calculated for multiple differentiation cycles (O'Hara & Mathews, 1981).

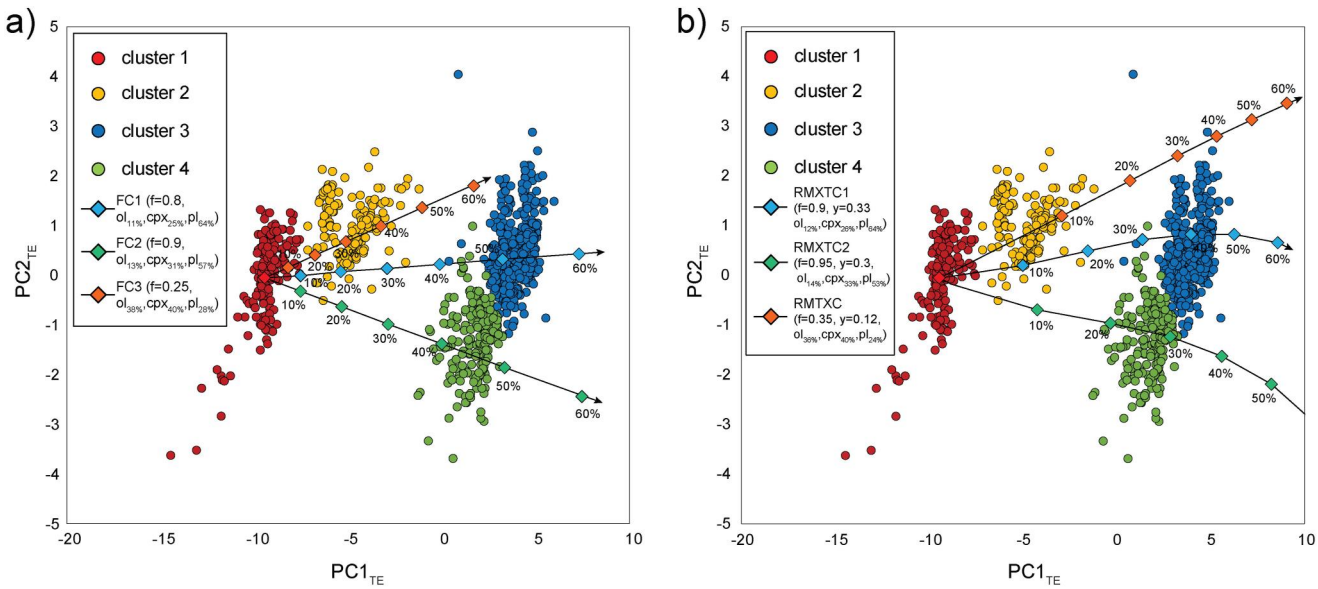

Figure 6. Differentiation trends in the $PC1_{TE}$-$PC2_{TE}$ compositional space for closed-system (a) and open-system (b) conditions. Vectors are calculated for fractional crystallization (FC; Equation 6), recharged, mixed, crystallized before tapped magma chambers (RMXTC; Equation 11) and recharged, mixed before tapped, crystallized magma chambers (RMTXC; Equation 13). Parameters fixed for each model are reported in the figure legend and represent the best case values defined by Monte Carlo simulations. Differentiation trends are shown for an increasing degree of crystallization (x). See Section 2 for further details on the modeling approach.

4. Discussions

4.1. Interpreting Principal Components and Clusters Through Magmatic Processes

Statistical principles behind PCA optimize the variance distribution by linearly combining the measured variables and defining a set of new orthogonal dimensions (see Section 2 for further details). In this respect, our data set provides the opportunity to integrate and compare multivariate statistics based separately on major and trace elements, yet subjected to the same data transformation and standardization procedure. This allows better interpretation of magma differentiation processes and addresses the merits and limitations of the two compositional data sets. PCA shows a steeper decline in system variance for principal components based on trace elements, while KCA identifies a higher number of clusters for trace elements than for major elements. This apparent dichotomy can be solved by performing a reification of the extracted principal components and interpreting the principal component scores for each cluster.

Loadings on $PC1_{ME}$ show both positive and negative signs for major element enrichment (e.g., SiO_2, FeO, Na_2O, and K_2O) and depletion (i.e., Al_2O_3, MgO, and CaO) in magmas, thereby reflecting the main differentiation processes controlling the Present-Day activity at Stromboli. The differentiation of *hp* matrix glasses is mostly governed by the crystallization of a phase assemblage dominated by plagioclase, whose stability is enhanced at the expense of clinopyroxene and olivine due to extensive cooling and degassing phenomena taking place in the shallower part of the *hp* reservoir (e.g., Di Stefano et al., 2020; Landi et al., 2004; Metrich et al., 2010). The *hp* reservoir is generally conceptualized as a largely crystalline body of magma, located at ∼1–4 km (e.g., Di Stefano et al., 2020; Landi et al., 2004; Petrone et al., 2022). This crustal region is persistently fed by inputs of more mafic and volatile-rich *lp*-magmas from a deeper (6 ∼ 9 km), dike-like reservoir, characterized by the crystallization of clinopyroxene and olivine (Di Stefano et al., 2020; Metrich et al., 2001; Petrone et al., 2022).

The highly incompatible character of K_2O in the phase assemblage controlling the liquid line of descent of magmas at Stromboli (e.g., Landi et al., 2022), coupled with its highest positive loading on $PC1_{ME}$ (Figure 2), supports the interpretation of $PC1_{ME}$ as a proxy for magma differentiation (Figure 1). Conversely, MnO and Na_2O contribute to most of the variance represented by $PC2_{ME}$ and $PC3_{ME}$, respectively (Figure 1c), but their isolated variations are difficult to reconcile with magma differentiation. It is nonetheless possible that $PC2_{ME}$ and $PC3_{ME}$ describe changing element partitioning during magma differentiation, driven by variable *P*-*T* conditions and mineral-melt compositions. Matrix glass compositions reflect the prevalent incorporation of Mn in olivine and

clinopyroxene during magma differentiation (Dunn, 1987), whereas the Na content in the residual melts is governed by plagioclase solid solution and its shifts toward the albite end-member with decreasing temperature and changing magma composition (e.g., Moschini et al., 2023). Nonetheless, the absence of detectable trends in $PC1_{ME}$-$PC2_{ME}$, $PC1_{ME}$-$PC3_{ME}$, and $PC1_{ME}$-$PC4_{ME}$ plots (Figures 2 and 4) hinders any attempt at reification for $PC2_{ME}$, $PC3_{ME}$, and $PC4_{ME}$, and hence negate their relation with magma differentiation. This is also expressed by probability density functions showing that $PC2_{ME}$, $PC3_{ME}$, and $PC4_{ME}$ scores display significant overlap between the different clusters, whereas only $PC1_{ME}$ scores substantially help the discernment of compositional clusters (Figure 2). This is a corollary of the principle that principal components cannot be a priori considered as representative of the physicochemical processes controlling the compositional variation in the original data set, and that reification is a prerequisite to obtain a meaningful PCA (Davis, 2002; Joliffe, 2002).

Loadings on $PC1_{TE}$ are, comparably to $PC1_{ME}$, divided between highly positive and highly negative, in response to the geochemical behavior of major and trace elements during the crystallization of the dominant phase assemblage. For instance, elements exhibiting positive loadings on $PC1_{TE}$ are incompatible in olivine, clinopyroxene and plagioclase, such as Rb and Zr (Figure 1d), with average partition coefficients comprised in the ranges of $K_{Rb}^{cpx,ol,pl} = 0.01 - 0.16$ and $K_{Zr}^{cpx,ol,pl} = 0.03 - 0.29$ (Table S4 in Supporting Information S1). On the other hand, the negative loadings for Cr, Ni, and Sr on $PC1_{TE}$ reflect their highly compatible behavior in clinopyroxene, olivine and plagioclase crystals, respectively ($K_{Cr}^{cpx} = 1.66 - 40.2$, $K_{Ni}^{ol} = 0.94 - 39.5$ and $K_{Sr}^{pl} = 1.29 - 6.35$). More complex geochemical effects are observed for V and Y, as these elements are either compatible or incompatible in the lattice site of clinopyroxene ($K_{V}^{cpx} = 0.08 - 3.41$; $K_{Y}^{cpx} = 0.2 - 1.27$), but invariably show positive loadings on $PC1_{TE}$. This is due to the fact that V and Y are highly incompatible in plagioclase ($K_{V}^{pl} = 0.03 - 0.14$; $K_{Y}^{pl} = 0 - 0.2$), whose crystallization dominates the geochemical transition from *lp* to *hp* magmas (e.g., Francalanci et al., 1989, 1999, 2013; Landi et al., 2004, 2022). Therefore, both $PC1_{TE}$ and $PC1_{ME}$ successfully outline the overall geochemical evolution of matrix glasses, ranging from negative to positive $PC1_{ME}$ and $PC1_{TE}$ scores as magma differentiation proceeds from *lp* to *hp* compositions, and transition through intermediate magmas (Figures 2 and 3).

Trace elements compatible with mafic phases (i.e., Sc, V, Cr, Co, and Ni) display positive loadings on $PC2_{TE}$ (Figure 1d), expressing its strong correlation with the crystallization of olivine and clinopyroxene. In contrast, incompatible trace elements (e.g., Rb, Zr, Nb, La, Th) exhibit negligible loadings on $PC2_{TE}$ (Figure 1d), suggesting a poor correlation with the extent of magma differentiation. The spatial distribution of $PC1_{TE}$-$PC2_{TE}$ scores reflects changes in the ratio of compatible to incompatible elements, allowing better discrimination of cluster 2_{TE} from cluster 1_{TE} and cluster 4_{TE} from cluster 3_{TE} (Figure 3). This variation may be assigned to variable mineral proportions in the crystallizing phase assemblage, as the differentiation of clusters 2_{TE} and 4_{TE} is characterized by higher clinopyroxene to plagioclase ratios in the fraction of crystalline residue, when compared to cluster 3_{TE} (Figure 5).

The observed relationship between $PC2_{TE}$ and $PC1_{TE}$, sharing non-zero loadings of the same trace elements, epitomizes the concept that principal components represent a set of orthogonal axes in the multivariate compositional space but are not strictly independent from one another as they incorporate the variance of multiple original variables (Iwamori et al., 2017; Joliffe, 2002). Although distinct principal components may share loadings from the same original variables, they may depict uncorrelated variations in the multicomponent space (Joliffe, 2002). This property of principal components may explain the negligible effect of magma differentiation on $PC2_{TE}$, in spite of the loadings for compatible trace elements shared with $PC1_{TE}$. A similar conclusion can be drawn for $PC4_{TE}$, whose scores exhibit significant variations between clusters, and correlate with $PC1_{TE}$ scores (Figure 4). It is observed that $PC4_{TE}$ scores of cluster 2_{TE} are lower than those of cluster 1_{TE}, while they slightly increase in the more differentiated clusters 3_{TE} and 4_{TE}. Since Sr constitutes the main loading on $PC4_{TE}$, the variation in Sr concentration along this principal component is orthogonal to $PC1_{TE}$, the latter describing the differentiation of magmas. Therefore, the score dispersion within the $PC1_{TE}$-$PC4_{TE}$ space may either reflect the lower abundance of plagioclase in the phase assemblage determining the differentiation of cluster 2_{TE} with respect to clusters 3_{TE} and 4_{TE} (Figure 5), or the increased compatibility of Sr in plagioclase as magma differentiation proceeds toward clusters 3_{TE} and 4_{TE} and the feldspar solid solution becomes more albitic (Bindeman et al., 1998; Landi et al., 2004; Moschini et al., 2023; Pontesilli et al., 2023).

Principal component scores in the $PC1_{TE}$-$PC3_{TE}$ space also exhibited significant variability within and between clusters (Figure 4). The only element that appreciably contributes to $PC3_{TE}$ is Li by virtue of its loading on this

principal component that is much higher than those of other elements (Figure 1d). Li mostly behaves as an incompatible element in the mineral assemblage of Stromboli magmas (Pontesilli et al., 2023), showing moderately low mineral-melt partition coefficients for clinopyroxene, olivine, and plagioclase ($K_{Li}^{cpx,ol,pl} = 0.29 - 0.38$ on average). The incompatible behavior of Li during magma differentiation is also highlighted by its positive loading on $PC1_{TE}$ (Figure 1d). The increase in $PC1_{TE}$ and the decrease in $PC3_{TE}$ scores thus reflect increasing Li contents in the residual melt and the corresponding matrix glass (Figure 4). On the other hand, the intra-cluster variation of $PC3_{TE}$ scores observed for cluster 3_{TE}, and marginally by cluster 4_{TE}, cannot be attributed to magma differentiation, as no correlation holds with $PC1_{TE}$ (Figure 4). According to Pontesilli et al. (2023), small amounts of microlite crystallization induced by the ascent and decompression of *hp* magmas determine a large variability of Li in the groundmass glass, owing to its high cation mobility during degassing phenomena, thereby explaining the dispersion of $PC3_{TE}$ scores observed for clusters 3_{TE} and 4_{TE} (Figure 4).

4.2. Implications for Plumbing System Architecture and Magma Dynamics

Despite the overall similarities between different modeling results (Figure 5), the fraction of crystalline residue x estimated for open-system conditions (30%–45%) is lower than that obtained for closed-system conditions (40%–55%) to attain comparable $PC1_{TE}$ scores for *hp* magmas. This result agrees with the underlying principles of steady state magmatic systems, wherein incompatible elements increase more rapidly when open-system conditions occur (Albarede, 1985; Lee et al., 2014; O'Hara, 1977). On the other hand, compatible elements are less influenced by open-system dynamics, as displayed by the substantial overlaps between trace element concentrations of clusters 3_{TE} and 4_{TE} (Figure 3 and Figure S3 in Supporting Information S1). The lower degree of crystallization through an open-system differentiation in the *hp* reservoir is consistent with models of magma mobility and hence eruptability that predict a rheological threshold of ~50% crystallinity separating suspension-like and mush-like behaviors (e.g., Dufek & Bachmann, 2010; Ellis et al., 2023; Forni et al., 2018; Hildreth, 2004).

The degree of dissimilarity between results of open- and closed-system melt differentiation scenarios may be expressed by the sum of x and y, which corresponds to the fraction of magma recharged at each differentiation cycle z (O'Hara & Mathews, 1981; see Section 2 for further details). This is estimated in the ranges 0.40–0.75 and 0.50–0.95 for clusters 4_{TE} and 3_{TE}, respectively (Figure S9 in Supporting Information S1). As z values approach 1, the maximum value this parameter can assume, complete turnover of the magmatic reservoir is predicted at each differentiation cycle. As such, melt differentiation in the steady state system predicted by Equations 11 and 13 reduces to the simple FC case of Equation 6 (O'Hara & Mathews, 1981). In other words, as the volume of magma replenishing the reservoir over the differentiation cycle approaches that of the whole reservoir, then an open-system magma differentiation approximates the closed-system behavior. Accordingly, the close similarities between melt compositions from open- and closed-system modeling are expressed by the high values of z in open-system scenarios. The implication is that most of the *hp* reservoir is completely rejuvenated within an average of 1–2 differentiation cycles according to geochemical modeling results based on clusters 3_{TE} and 4_{TE}.

In order for this hypothesis to hold true, the frequency of magma recharge episodes to the *hp* reservoir needs to be on the same timescales as those estimated for magma turnover in the shallow plumbing system. Average magma residence times in the *hp* reservoir are estimated on the basis of $^{87}Sr/^{86}Sr$ systematics to range between 10 and 30 years, implying a converted reservoir volume of 0.04–0.3 km^3 (Francalanci et al., 1999). Similar timescales are provided by Bragagni et al. (2014) through U-series disequilibria, with a best-case residence time estimated at 5 years out of the larger range of 2–55 years, on which a magmatic reservoir of 0.02–0.09 km^3 was estimated. These relatively long residence times relate to the deepest part of the *hp* reservoir, where mixing between *hp* and *lp* magmas and the crystalline mush at depths of 2–4 km are proposed (Bragagni et al., 2014). Based on degassing-controlled ^{210}Pb–^{226}Ra disequilibria, shorter residence times of ~0.7–3 years are instead estimated for the shallower part of the *hp* reservoir (Gauthier & Condomines, 1999), also in agreement with timescales for plagioclase growth and dissolution in the upper conduit at Stromboli (Agostini et al., 2013). Notably, historical data and temporal models suggest that the average frequency for paroxysmal eruptions was of one event every 4 years, during the last 140 years (Bevilacqua et al., 2020). The ubiquitous eruption of mafic *lp* magma during paroxysmal events indicates that 4 years actually represent the lower limit for the frequency of mafic recharge episodes to the *hp* reservoir since *lp* magma is also involved in some major eruptions and some recharge episodes may not lead to violent explosive scenarios (e.g., Landi et al., 2022; Petrone et al., 2022; Voloschina et al., 2023). Therefore, comparison of independent constraints on average residence times and recharge frequency indicates

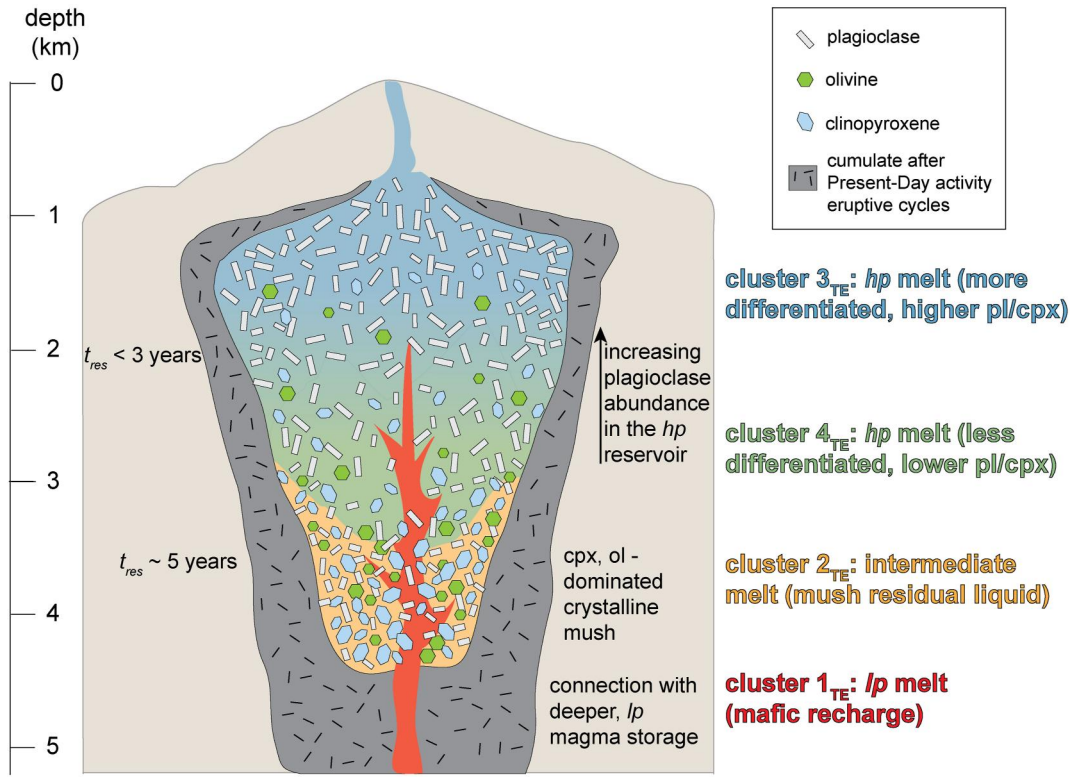

Figure 7. Schematic reconstruction of the shallow magma storage zone at Stromboli, as illustrated by multivariate statics and open-system differentiation modeling results. Cluster 2_{TE} includes intermediate melt compositions, representing the residual liquid of olivine-clinopyroxene-dominated crystalline mush located toward the bottom of the *hp* reservoir. In this region, intermediate melts originate by mixing between the residual liquid of the crystalline mush and *lp* melts. Cluster 1_{TE} identifies mafic and crystal-poor *lp* magmas rising from depth and injecting into the more differentiated and crystal-rich *hp* reservoir. Both clusters 4_{TE} and 3_{TE} refer to *hp* melts that become more differentiated toward the top of the *hp* reservoir, where residence timescales are estimated to decrease and magma differentiation is strongly dominated by plagioclase crystallization. Here, a high fraction of magma recharged during each differentiation cycle determines the short residence time of magma. The gray field indicates crystal accumulation from past to present differentiation cycles.

that timescales of *lp* recharges are on the same order of magnitude or slightly shorter than those of magma rejuvenation in the *hp* reservoir. This observation is in agreement with the open-system modeling results, indicating that these recharge episodes set forth the consecution of differentiation cycles.

Furthermore, this implies that the volume of *lp* magma batches supplied in the months to days before each paroxysmal event (Di Stefano et al., 2020; Petrone et al., 2018, 2022) is equal to or slightly lower than that recharging the system over an entire differentiation cycle, estimated to represent 40%–95% of the eruptible volume of the *hp* reservoir. Hence, an increase in magma residence time with depth in the *hp* reservoir corresponds to a decrease in the fraction of magma replenished during a differentiation cycle because more cycles are needed to completely rejuvenate the system. Modeling results based on *hp* compositions belonging to cluster 4_{TE} hints at a lower percentage of magma recharged over a differentiation cycle (40%–75%) when compared to those based on cluster 3_{TE} (45%–90%). Moreover, cluster 4_{TE} results from a lower degree of crystallization and lower plagioclase to clinopyroxene ratio, as supported by open- and closed-system modeling results (Figure 5). It can be concluded that the cluster 4_{TE} represents slightly more primitive magmas originating from deeper regions of the *hp* reservoir with respect to more evolved magmas represented by the cluster 3_{TE}. This latter cluster illustrates the transition toward a shallower and plagioclase-rich part of the *hp* reservoir, where higher fractions of magma renewed at each differentiation cycle are stored over shorter residence times (Figure 7).

Cluster 2_{TE} brackets intermediate glass compositions, interpreted as the product of mixing and subsequent crystallization between the ascending *lp* magma and a least evolved *hp* magma residing in a transitional magmatic environment (Landi et al., 2008, 2022). Modeling results indicate that matrix glasses from cluster 2_{TE} are

produced by the crystallization of mafic phases (clinopyroxene and olivine) via in situ crystallization ($f < 0.5$), which is typical of highly crystalline environments such as the margins of convecting magma chambers, where crystallization proceeds separately from the main reservoir (Langmuir, 1989). Intermediate magma compositions are thus interpreted as the result of continued mixing and in situ crystallization in a mush-like environment located in close proximity to the bottom of the *hp* reservoir (~4 km; Figure 7), where the continuous supply of mafic magmas keeps the residual melt on the olivine-clinopyroxene cotectic (Francalanci et al., 1999, 2012; Landi et al., 2022; Pichavant et al., 2009). Interestingly, lower z values (10%–30%) from open-system modeling of cluster 2_{TE} imply much longer residence times with respect to *hp* magmas (clusters 3_{TE} and 4_{TE}), also explaining the disagreement between open- and closed-system modeling results for cluster 2_{TE} (Figure 5). Different modal abundances, degree of crystallization and fraction of liquid returning from the solidification front, estimated for cluster 2_{TE} with respect to clusters 3_{TE} and $4_{TE,}$ thus reflect the transition from a mush-like environment to a suspension-like upper region of the *hp* reservoir (Figure 7). In such environment, efficient crystal-melt separation is also supported by the fact that f approaches 1 for clusters 3_{TE} and 4_{TE}, thereby approximating melt evolution along closed-system fractional crystallization trends (Figure 6).

5. Conclusions

In this study, a large compositional data set based on major and trace analyses of matrix glasses erupted at Stromboli over the last 20 years has been interrogated through a multifaceted approach including principal component analysis (PCA), K-means cluster analysis (KCA) and kernel density estimation (KDE). Comparison between open- and closed-system differentiation models outlines that the short residence time of magmas within the shallow reservoir of Stromboli determines variable degrees of melt differentiation that approximate simple fractional crystallization trends for the most evolved melt compositions. This compositional effect is interpreted as the transition from a mush-like environment at the bottom of the plumbing system toward eruptible melts stored in the upper part of the magmatic reservoir. The dichotomy of our modeling results shows that care should be taken when applying geochemical modeling equations to volcanic systems without considering the spatial and temporal evolution of erupted melts. The modeling approach should be based on the conceptual model of the differentiation processes being investigated and be informed by other data such as crystal textures and magmatic timescales. By combining an iterative modeling approach and multivariate statistical analyses, we can unbiasedly constrain the most important parameters controlling magma differentiation and better interrogate large analytical data sets and their subset compositional variations. Specifically, results from PCA indicate that changes in trace elements in erupted matrix glasses are more informative than changes in major elements for defining compositional clusters and thus interpreting magmatic processes. Nonetheless, it is crucial that transformed variables can be robustly interpreted in terms of the igneous processes at play to allow for a meaningful clustering solution. The implementation of petrological monitoring practices and automatic samplers in areas of active volcanic output are instrumental in the collection of large data bases and hence in constraining petrological models via multivariate approaches.

Acknowledgments
The authors are grateful to Patrizia Landi and Claudia D'Oriano for the insightful conversations on matrix glass compositions at Stromboli. Thanks also go to Marcel Guillong and Lorenzo Tavazzani for assistance during LA-ICPMS analyses. The authors acknowledge the following projects: IR0000025—"Monitoring Earth's Evolution and Tectonics," MEET—MUR Grant: D53C22001400005 to AP, FDF and PS; INGV Departmental Strategic Project UNO to AP, PS, EDB, DA, JT and MN; PRIN MUR Grant 2022N4FBAA to EDB and SM; Swiss National Science Foundation Grant 200020-197040 to BE and OB. MB is grateful for research and study leave support from the Division of Sciences, University of Otago. Editor Marie Edmonds is acknowledged for the careful editorial handling and for reviewing the manuscript. The authors are grateful to anonymous reviewers for careful reading and the constructive comments provided.

Conflict of Interest

The authors declare no conflicts of interest relevant to this study.

Data Availability Statement

Matrix glass compositions, including major and trace element concentrations, analytical precision and accuracy based on secondary standards, as well as principal component scores, data clustering for each point analysis, partition coefficient values from literature, including the complete reference list, and results of differentiation modeling, are available in Supporting Information S1 (Pontesilli, 2023).

References

Agostini, C., Fortunati, A., Arzilli, F., Landi, P., & Carroll, M. R. (2013). Kinetics of crystal evolution as a probe to magmatism at Stromboli (Aeolian Archipelago, Italy). *Geochimica et Cosmochimica Acta*, *110*, 135–151. https://doi.org/10.1016/j.gca.2013.02.027

Aitchison, J. (1999). Logratios and natural laws in compositional data analysis. *Mathematical Geology*, *31*(5), 563–580. https://doi.org/10.1023/A:1007568008032

Albarede, F. (1985). Regime and trace-element evolution of open magma chambers. *Nature*, *318*(6044), 356–358. https://doi.org/10.1038/318356a0

Allègre, C. J., & Minster, J. F. (1978). Quantitative models of trace element behavior in magmatic processes. *Earth and Planetary Science Letters*, *38*(1), 1–25. https://doi.org/10.1016/0012-821X(78)90123-1

Andronico, D., Corsaro, R. A., Cristaldi, A., & Polacci, M. (2008). Characterizing high energy explosive eruptions at Stromboli volcano using multidisciplinary data: An example from the 9 January 2005 explosion. *Journal of Volcanology and Geothermal Research*, *176*(4), 541–550. https://doi.org/10.1016/j.jvolgeores.2008.05.011

Andronico, D., Del Bello, E., D'Oriano, C., Landi, P., Pardini, F., Scarlato, P., et al. (2021). Uncovering the eruptive patterns of the 2019 double paroxysm eruption crisis of Stromboli volcano. *Nature Communications*, *12*(1), 4213. https://doi.org/10.1038/s41467-021-24420-1

Armienti, P., Francalanci, L., & Landi, P. (2007). Textural effects of steady state behaviour of the Stromboli feeding system. *Journal of Volcanology and Geothermal Research*, *160*(1), 86–98. https://doi.org/10.1016/j.jvolgeores.2006.05.004

Barberi, F., Rosi, M., & Sodi, A. (1993). Volcanic hazard assessment at Stromboli based on a review of historical data. *Acta Vulcanologica*, *3*, 173–187.

Bertagnini, A., Di Roberto, A., & Pompilio, M. (2011). Paroxysmal activity at Stromboli: Lessons from the past. *Bulletin of Volcanology*, *73*(9), 1229–1243. https://doi.org/10.1007/s00445-011-0470-3

Bevilacqua, A., Bertagnini, A., Pompilio, M., Landi, P., Del Carlo, P., Di Roberto, A., et al. (2020). Major explosions and paroxysms at Stromboli (Italy): A new historical catalog and temporal models of occurrence with uncertainty quantification. *Scientific Reports*, *10*(1), 17357. https://doi.org/10.1038/s41598-020-74301-8

Bindeman, I. N., Davis, A. M., & Drake, M. J. (1998). Ion microprobe study of plagioclase-basalt partition experiments at natural concentration levels of trace elements. *Geochimica et Cosmochimica Acta*, *62*(7), 1175–1193. https://doi.org/10.1016/S0016-7037(98)00047-7

Blundy, J., & Cashman, K. (2008). Petrologic reconstruction of magmatic system variables and processes. *Reviews in Mineralogy and Geochemistry*, *69*(1), 179–239. https://doi.org/10.2138/rmg.2008.69.6

Bragagni, A., Avanzinelli, R., Freymuth, H., & Francalanci, L. (2014). Recycling of crystal mush-derived melts and short magma residence times revealed by U-series disequilibria at Stromboli volcano. *Earth and Planetary Science Letters*, *404*, 206–219. https://doi.org/10.1016/j.epsl.2014.07.028

Davis, J. C. (2002). *Statistics and data analysis in geology* (3rd ed.). Wiley. Retrieved from https://www.wiley.com/en-br/Statistics+and+Data+Analysis+in+Geology%2C+3rd+Edition-p-9780471172758

Di Fiore, F., Vona, A., Mollo, S., Nazzari, M., Giordano, G., & Romano, C. (2023). Experimental insights on the shear-induced crystallization of a phonotephrite magma. *Chemical Geology*, *637*, 121682. https://doi.org/10.1016/j.chemgeo.2023.121682

Di Fiore, F., Vona, A., Scarani, A., Giordano, G., Romano, C., Giordano, D., et al. (2023). Experimental constraints on the rheology of lavas from 2021 Cumbre Vieja eruption (La Palma, Spain). *Geophysical Research Letters*, *50*(4), e2022GL100970. https://doi.org/10.1029/2022GL100970

Ding, C., & He, X. (2004). K-means clustering via principal component analysis. In *Proceedings of the twenty-first international conference on Machine learning* (p. 29). Association for Computing Machinery. https://doi.org/10.1145/1015330.1015408

Di Renzo, V., Corsaro, R. A., Miraglia, L., Pompilio, M., & Civetta, L. (2019). Long and short-term magma differentiation at Mt. Etna as revealed by Sr-Nd isotopes and geochemical data. *Earth-Science Reviews*, *190*, 112–130. https://doi.org/10.1016/j.earscirev.2018.12.008

Di Stefano, F., Mollo, S., Ubide, T., Petrone, C. M., Caulfield, J., Scarlato, P., et al. (2020). Mush cannibalism and disruption recorded by clinopyroxene phenocrysts at Stromboli volcano: New insights from recent 2003–2017 activity. *Lithos*, *360–361*, 105440. https://doi.org/10.1016/j.lithos.2020.105440

Dufek, J., & Bachmann, O. (2010). Quantum magmatism: Magmatic compositional gaps generated by melt-crystal dynamics. *Geology*, *38*(8), 687–690. https://doi.org/10.1130/G30831.1

Dunn, T. (1987). Partitioning of Hf, Lu, Ti, and Mn between olivine, clinopyroxene and basaltic liquid. *Contributions to Mineralogy and Petrology*, *96*(4), 476–484. https://doi.org/10.1007/BF01166692

Edmonds, M., Liu, E. J., & Cashman, K. V. (2022). Open-vent volcanoes fuelled by depth-integrated magma degassing. *Bulletin of Volcanology*, *84*(3), 28. https://doi.org/10.1007/s00445-021-01522-8

Ellis, B. S., Szymanowski, D., Harris, C., Tollan, P. M. E., Neukampf, J., Guillong, M., et al. (2022). Evaluating the potential of rhyolitic glass as a lithium source for brine deposits. *Economic Geology*, *117*(1), 91–105. https://doi.org/10.5382/econgeo.4866

Ellis, B. S., Wolff, J. A., Szymanowski, D., Forni, F., Cortes-Calderon, E. A., & Bachmann, O. (2023). Cumulate recycling in igneous systems: The volcanic record. *Lithos*, *456–457*, 107284. https://doi.org/10.1016/j.lithos.2023.107284

Everitt, B. S., Landau, S., Leese, M., & Stahl, D. (2011). *Cluster analysis*. John Wiley & Sons.

Forni, F., Petricca, E., Bachmann, O., Mollo, S., De Astis, G., & Piochi, M. (2018). The role of magma mixing/mingling and cumulate melting in the Neapolitan Yellow Tuff caldera-forming eruption (Campi Flegrei, Southern Italy). *Contributions to Mineralogy and Petrology*, *173*(6), 45. https://doi.org/10.1007/s00410-018-1471-4

Francalanci, L., Avanzinelli, R., Nardini, I., Tiepolo, M., Davidson, J. P., & Vannucci, R. (2012). Crystal recycling in the steady-state system of the active Stromboli volcano: A 2.5-ka story inferred from in situ Sr-isotope and trace element data. *Contributions to Mineralogy and Petrology*, *163*(1), 109–131. https://doi.org/10.1007/s00410-011-0661-0

Francalanci, L., Lucchi, F., Keller, J., De Astis, G., & Tranne, C. A. (2013). Chapter 13 Eruptive, volcano-tectonic and magmatic history of the Stromboli volcano (north-eastern Aeolian archipelago). *Geological Society, London, Memoirs*, *37*(1), 397–471. https://doi.org/10.1144/M37.13

Francalanci, L., Manetti, P., & Peccerillo, A. (1989). Volcanological and magmatological evolution of Stromboli volcano (Aeolian Islands): The roles of fractional crystallization, magma mixing, crustal contamination and source heterogeneity. *Bulletin of Volcanology*, *51*(5), 355–378. https://doi.org/10.1007/BF01056897

Francalanci, L., Tommasini, S., & Conticelli, S. (2004). The volcanic activity of Stromboli in the 1906–1998 AD period: Mineralogical, geochemical and isotope data relevant to the understanding of the plumbing system. *Journal of Volcanology and Geothermal Research*, *131*(1), 179–211. https://doi.org/10.1016/S0377-0273(03)00362-7

Francalanci, L., Tommasini, S., Conticelli, S., & Davies, G. R. (1999). Sr isotope evidence for short magma residence time for the 20th century activity at Stromboli volcano, Italy. *Earth and Planetary Science Letters*, *167*(1), 61–69. https://doi.org/10.1016/S0012-821X(99)00013-8

Gauthier, P.-J., & Condomines, M. (1999). 210Pb–226Ra radioactive disequilibria in recent lavas and radon degassing: Inferences on the magma chamber dynamics at Stromboli and Merapi volcanoes. *Earth and Planetary Science Letters*, *172*(1), 111–126. https://doi.org/10.1016/S0012-821X(99)00195-8

Hildreth, W. (2004). Volcanological perspectives on Long Valley, Mammoth Mountain, and Mono Craters: Several contiguous but discrete systems. *Journal of Volcanology and Geothermal Research*, *136*(3), 169–198. https://doi.org/10.1016/j.jvolgeores.2004.05.019

Iwamori, H., Yoshida, K., Nakamura, H., Kuwatani, T., Hamada, M., Haraguchi, S., & Ueki, K. (2017). Classification of geochemical data based on multivariate statistical analyses: Complementary roles of cluster, principal component, and independent component analyses. *Geochemistry, Geophysics, Geosystems*, *18*(3), 994–1012. https://doi.org/10.1002/2016GC006663

Jochum, K. P., Nohl, U., Herwig, K., Lammel, E., Stoll, B., & Hofmann, A. W. (2005). GeoReM: A new geochemical database for reference materials and isotopic standards. *Geostandards and Geoanalytical Research*, *29*(3), 333–338. https://doi.org/10.1111/j.1751-908X.2005.tb00904.x

Joliffe, I. T. (2002). *Principal component analysis*. Springer-Verlag. https://doi.org/10.1007/b98835

Kuritani, T., Tanaka, M., Yokoyama, T., Nakagawa, M., & Matsumoto, A. (2016). Intensive hydration of the Wedge Mantle at the Kuril arc–NE Japan arc Junction: Implications from mafic lavas from Usu Volcano, Northern Japan. *Journal of Petrology*, *57*(6), 1223–1240. https://doi.org/10.1093/petrology/egw038

La Felice, S., & Landi, P. (2011). A spatter-forming, large-scale paroxysm at Stromboli Volcano (Aeolian Islands, Italy): Insight into magma evolution and eruption dynamics. *Bulletin of Volcanology*, *73*(9), 1393–1406. https://doi.org/10.1007/s00445-011-0476-x

Landi, P., D'Oriano, C., Petrelli, M., Nazzari, M., & Andronico, D. (2022). Inferences on the magmatic plumbing system at Stromboli volcano (Italy) from trace element geochemistry of matrix glasses and minerals in different types of explosive eruptions. *Contributions to Mineralogy and Petrology*, *177*(10), 96. https://doi.org/10.1007/s00410-022-01962-1

Landi, P., Métrich, N., Bertagnini, A., & Rosi, M. (2004). Dynamics of magma mixing and degassing recorded in plagioclase at Stromboli (Aeolian Archipelago, Italy). *Contributions to Mineralogy and Petrology*, *147*(2), 213–227. https://doi.org/10.1007/s00410-004-0555-5

Landi, P., Métrich, N., Bertagnini, A., & Rosi, M. (2008). Recycling and "re-hydration" of degassed magma inducing transient dissolution/crystallization events at Stromboli (Italy). *Journal of Volcanology and Geothermal Research*, *174*(4), 325–336. https://doi.org/10.1016/j.jvolgeores.2008.02.013

Langmuir, C. H. (1989). Geochemical consequences of in situ crystallization. *Nature*, *340*(6230), 199–205. https://doi.org/10.1038/340199a0

Lee, C.-T. A., Lee, T. C., & Wu, C.-T. (2014). Modeling the compositional evolution of recharging, evacuating, and fractionating (REFC) magma chambers: Implications for differentiation of arc magmas. *Geochimica et Cosmochimica Acta*, *143*, 8–22. https://doi.org/10.1016/j.gca.2013.08.009

Le Maitre, R. W. (1982). *Numerical petrology: Statistical interpretation of geochemical data*. Elsevier.

Liu, E. J., Cashman, K. V., Miller, E., Moore, H., Edmonds, M., Kunz, B. E., et al. (2020). Petrologic monitoring at Volcán de Fuego, Guatemala. *Journal of Volcanology and Geothermal Research*, *405*, 107044. https://doi.org/10.1016/j.jvolgeores.2020.107044

Marriott, F. H. C. (1974). *The interpretation of multiple observations*. Academic Press.

Métrich, N., Bertagnini, A., & Di Muro, A. (2010). Conditions of magma storage, degassing and ascent at Stromboli: New insights into the volcano plumbing system with inferences on the eruptive dynamics. *Journal of Petrology*, *51*(3), 603–626. https://doi.org/10.1093/petrology/egp083

Métrich, N., Bertagnini, A., Landi, P., & Rosi, M. (2001). Crystallization driven by decompression and water loss at Stromboli Volcano (Aeolian Islands, Italy). *Journal of Petrology*, *42*(8), 1471–1490. https://doi.org/10.1093/petrology/42.8.1471

Mollo, S., Pontesilli, A., Moschini, P., Palummo, F., Taddeucci, J., Andronico, D., et al. (2022). Modeling the crystallization conditions of clinopyroxene crystals erupted during February–April 2021 lava fountains at Mt. Etna: Implications for the dynamic transfer of magmas. *Lithos*, *420–421*, 106710. https://doi.org/10.1016/j.lithos.2022.106710

Moschini, P., Mollo, S., Pontesilli, A., Nazzari, M., Petrone, C. M., Fanara, S., et al. (2023). A review of plagioclase growth rate and compositional evolution in mafic alkaline magmas: Guidelines for thermometry, hygrometry, and timescales of magma dynamics at Stromboli and Mt. Etna. *Earth-Science Reviews*, *240*, 104399. https://doi.org/10.1016/j.earscirev.2023.104399

National Academies of Sciences, E. (2017). *Volcanic eruptions and their repose, unrest, precursors, and timing*. National Academies of Sciences. https://doi.org/10.17226/24650

O'Hara, M. J. (1977). Geochemical evolution during fractional crystallisation of a periodically refilled magma chamber. *Nature*, *266*(5602), 503–507. https://doi.org/10.1038/266503a0

O'Hara, M. J., & Herzberg, C. (2002). Interpretation of trace element and isotope features of basalts: Relevance of field relations, petrology, major element data, phase equilibria, and magma chamber modeling in basalt petrogenesis. *Geochimica et Cosmochimica Acta*, *66*(12), 2167–2191. https://doi.org/10.1016/S0016-7037(02)00852-9

O'Hara, M. J., & Mathews, R. E. (1981). Geochemical evolution in an advancing, periodically replenished, periodically tapped, continuously fractionated magma chamber. *Journal of the Geological Society*, *138*(3), 237–277. https://doi.org/10.1144/gsjgs.138.3.0237

Petrone, C. M., Braschi, E., Francalanci, L., Casalini, M., & Tommasini, S. (2018). Rapid mixing and short storage timescale in the magma dynamics of a steady-state volcano. *Earth and Planetary Science Letters*, *492*, 206–221. https://doi.org/10.1016/j.epsl.2018.03.055

Petrone, C. M., Mollo, S., Gertisser, R., Buret, Y., Scarlato, P., Del Bello, E., et al. (2022). Magma recharge and mush rejuvenation drive paroxysmal activity at Stromboli volcano. *Nature Communications*, *13*(1), 7717. https://doi.org/10.1038/s41467-022-35405-z

Pichavant, M., Di Carlo, I., Le Gac, Y., Rotolo, S. G., & Scaillet, B. (2009). Experimental constraints on the deep magma feeding system at Stromboli volcano, Italy. *Journal of Petrology*, *50*(4), 601–624. https://doi.org/10.1093/petrology/egp014

Pontesilli, A. (2023). Supplementary Data to Pontesilli et al 2023 manuscript [Dataset]. Zenodo. https://doi.org/10.5281/zenodo.10277932

Pontesilli, A., Brenna, M., Mollo, S., Masotta, M., Nazzari, M., Le Roux, P., & Scarlato, P. (2022). Trachyte-phonolite transition at Dunedin Volcano: Fingerprints of magma plumbing system maturity and mush evolution. *Lithos*, *408–409*, 106545. https://doi.org/10.1016/j.lithos.2021.106545

Pontesilli, A., Del Bello, E., Scarlato, P., Mollo, S., Ellis, B., Andronico, D., et al. (2023). The efficacy of high frequency petrological investigation at open-conduit volcanoes: The case of May 11 2019 explosions at southwestern and northeastern craters of Stromboli. *Lithos*, *454–455*, 107255. https://doi.org/10.1016/j.lithos.2023.107255

Ragland, P. C., Conley, J. F., Parker, W. C., & Von Orman, J. A. (1997). Use of principal components analysis in petrology: An example from the Martinsville igneous complex, Virginia, U.S.A. *Mineralogy and Petrology*, *60*(3), 165–184. https://doi.org/10.1007/BF01173708

Rollinson, H. R. (1993). *Using geochemical data: Evaluation, presentation, interpretation*. Routledge.

Rosi, M., Bertagnini, A., & Landi, P. (2000). Onset of the persistent activity at Stromboli Volcano (Italy). *Bulletin of Volcanology*, *62*(4), 294–300. https://doi.org/10.1007/s004450000098

Rosi, M., Pistolesi, M., Bertagnini, A., Landi, P., Pompilio, M., & Di Roberto, A. (2013). Chapter 14 Stromboli volcano, Aeolian Islands (Italy): Present eruptive activity and hazards. *Geological Society, London, Memoirs*, *37*(1), 473–490. https://doi.org/10.1144/M37.14

Schiavon, B., Mollo, S., Pontesilli, A., Del Bello, E., Nazzari, M., & Scarlato, P. (2023). Plagioclase crystal size distribution parameterization: A tool for tracking magma dynamics at Stromboli. *Lithos*, *446–447*, 107143. https://doi.org/10.1016/j.lithos.2023.107143

Silverman, B. W. (1986). *Density estimation for statistics and data analysis*. Routledge. https://doi.org/10.1201/9781315140919

Spina, L., Del Bello, E., Ricci, T., Taddeucci, J., & Scarlato, P. (2021). Multi-parametric characterization of explosive activity at Batu Tara Volcano (Flores Sea, Indonesia). *Journal of Volcanology and Geothermal Research*, *413*, 107199. https://doi.org/10.1016/j.jvolgeores.2021.107199

St C. O'Neill, H., & Jenner, F. E. (2012). The global pattern of trace-element distributions in ocean floor basalts. *Nature*, *491*(7426), 698–704. https://doi.org/10.1038/nature11678

Taddeucci, J., Scarlato, P., Andronico, D., Ricci, T., Civico, R., Del Bello, E., et al. (2023). The Explosive Activity of the 2021 Tajogaite Eruption (La Palma, Canary Islands, Spain). *Geochemistry, Geophysics, Geosystems*, *24*(6), e2023GC010946. https://doi.org/10.1029/2023GC010946

Thy, P., & Esbensen, K. H. (1993). Seafloor spreading and the ophiolitic sequences of the Troodos Complex: A principal component analysis of lava and dike compositions. *Journal of Geophysical Research*, *98*(B7), 11799–11805. https://doi.org/10.1029/93JB00695

Ubide, T., Galé, C., Arranz, E., Lago, M., & Larrea, P. (2014). Clinopyroxene and amphibole crystal populations in a lamprophyre sill from the Catalonian Coastal Ranges (NE Spain): A record of magma history and a window to mineral-melt partitioning. *Lithos*, *184–187*, 225–242. https://doi.org/10.1016/j.lithos.2013.10.029

Ubide, T., & Kamber, B. S. (2018). Volcanic crystals as time capsules of eruption history. *Nature Communications*, *9*(1), 326. https://doi.org/10.1038/s41467-017-02274-w

Ubide, T., Márquez, Á., Ancochea, E., Huertas, M. J., Herrera, R., Coello-Bravo, J. J., et al. (2023). Discrete magma injections drive the 2021 La Palma eruption. *Science Advances*, *9*(27), eadg4813. https://doi.org/10.1126/sciadv.adg4813

Ueki, K., & Iwamori, H. (2017). Geochemical differentiation processes for arc magma of the Sengan volcanic cluster, Northeastern Japan, constrained from principal component analysis. *Lithos*, *290–291*, 60–75. https://doi.org/10.1016/j.lithos.2017.08.001

Voloschina, M., Métrich, N., Bertagnini, A., Marianelli, P., Aiuppa, A., Ripepe, M., & Pistolesi, M. (2023). Explosive eruptions at Stromboli volcano (Italy): A comprehensive geochemical view on magma sources and intensity range. *Bulletin of Volcanology*, *85*(6), 34. https://doi.org/10.1007/s00445-023-01647-y

Zaiontz, C. (2022). Release 8.0. Retrieved from www.real-statistics.com

Zieg, M. J., & Wallrich, B. M. (2018). Emplacement and differentiation of the Black Sturgeon Sill, Nipigon, Ontario: A principal component analysis. *Journal of Petrology*, *59*(12), 2385–2412. https://doi.org/10.1093/petrology/egy100